

## Journal Pre-proofs

The correlation of fractal dimension to fracture surface slope for fatigue crack initiation analysis under bending-torsion loading in high-strength steels

W. Macek, R. Branco, P. Podulka, R. Masoudi Nejad, J.D. Costa, J.A.M. Ferreira, C. Capela

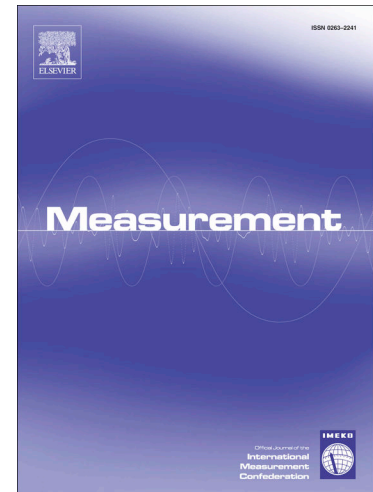
PII: S0263-2241(23)00733-9  
DOI: <https://doi.org/10.1016/j.measurement.2023.113169>  
Reference: MEASUR 113169

To appear in: *Measurement*

Received Date: 13 July 2022  
Revised Date: 16 May 2023  
Accepted Date: 3 June 2023

Please cite this article as: W. Macek, R. Branco, P. Podulka, R. Masoudi Nejad, J.D. Costa, J.A.M. Ferreira, C. Capela, The correlation of fractal dimension to fracture surface slope for fatigue crack initiation analysis under bending-torsion loading in high-strength steels, *Measurement* (2023), doi: <https://doi.org/10.1016/j.measurement.2023.113169>

This is a PDF file of an article that has undergone enhancements after acceptance, such as the addition of a cover page and metadata, and formatting for readability, but it is not yet the definitive version of record. This version will undergo additional copyediting, typesetting and review before it is published in its final form, but we are providing this version to give early visibility of the article. Please note that, during the production process, errors may be discovered which could affect the content, and all legal disclaimers that apply to the journal pertain.



**The correlation of fractal dimension to fracture surface slope for fatigue crack initiation analysis under bending-torsion loading in high-strength steels****The correlation of fractal dimension to fracture surface slope for fatigue crack initiation analysis under bending-torsion loading in high-strength steels**

W. Macek<sup>a</sup>, R. Branco<sup>b</sup>, P. Podulka<sup>c</sup>, R. Masoudi Nejad<sup>d</sup>, J.D. Costa<sup>b</sup>, J.A.M. Ferreira<sup>b</sup>, C. Capela<sup>b,e</sup>

<sup>a</sup> Gdańsk University of Technology, Faculty of Mechanical Engineering and Ship Technology, Gdańsk, Poland

<sup>b</sup> University of Coimbra, CEMMPRE, Department of Mechanical Engineering, Coimbra, Portugal

<sup>c</sup> Rzeszow University of Technology, Faculty of Mechanical Engineering and Aeronautics, Rzeszów, Poland

<sup>d</sup> School of Mechanical and Electrical Engineering, University of Electronic Science and Technology of China, Chengdu, P. R. China

<sup>e</sup> ESTG, Department of Mechanical Engineering, Instituto Politécnico de Leiria, Leiria, Portugal

Keywords: fractography; fractal dimension; fracture; steel; bending-torsion fatigue; fatigue crack initiation.

**Highlights**

- Comparison of fractal dimension under bending-torsion loading is studied.
- Effect of fatigue crack initiation life on fractal dimension of fracture surface is evaluated.
- Bending moment to torsion moment ratios and maximum local von Mises equivalent stress affects fracture surface topography.
- Fatigue crack initiation life is successfully predicted from fracture surface parameters and maximum local von Mises stress.

**Abstract:**

In this study, the fractal dimension of fatigue fracture surfaces is investigated in order to find an alternative failure loading indicator. Some of many metrological factors are generalized by reducing the fracture surface structure to one factor and develop an entire fracture surface procedure by analyzing the impact of surface slope and calculation resolution. Three notched geometries are studied under cyclic bending-torsion: (i) 34CrNiMo6 high-strength steel bars with transverse blind holes; (ii) 34CrNiMo6 high-strength steel bars with lateral U-shaped notches; and (iii) 18Ni300 maraging steel hollow bars with transverse holes produced by selective laser melting. The surface topographies of fatigue fractures were measured with an optical profilometer. The bending-torsion ratio, maximum local von Mises equivalent stress and the number of cycles to crack initiation

are examined using the fractal dimension. Moreover, a comparison was also made for conventional surface topography parameters such as root mean square height and void volume. A fatigue crack initiation model based on surface topography and loading conditions is proposed. The model relies on the product of the maximum local von Mises equivalent stress and the fractal dimension divided by the root mean square height to void volume ratio. The results show that the fracture plane geometry, expressed by the fractal dimension  $D_f$ , can facilitate the estimation of post-failure loading history. In particular, the analysis based on the enclosing boxes method (EBM) is more accurate when it is used as an extra-fine resolution without any plane leveling.

## 1. Introduction

Box-counting methods [1,2] are the most popular methods of determining the fractal dimension, especially the enclosing boxes method (EBM) [3] which involves taking a set of points and calculating the enclosed area. This calculation is then iterated with boxes having different widths. However, fractals are taken into account in many issues and fields of science, such as biology [4] or geology [5], and is often successfully used where conventional metrology needs to be aided. We can also see the multitasking of fractal dimension on the example of Reddy and Rao [6], where it was also used in fatigue studies, but for probabilistic fracture mechanics analysis. Their model for failure probability prediction showed high accuracy in comparison to the results of Monte Carlo simulation. Also in the statistical application, Cui et al. [7] analyzed descriptors correlation, including fractal dimension, for specific physical property prediction of heterogeneous materials.

Surface preparation for calculating topographic parameters is very important in metrology and is described in detail in several standards, such as the ISO 3274 [8] and the ISO 16610-21 [9]. Inter alia, the microroughness  $\lambda_s$  must be removed along with the form or slope  $\lambda_c$ , using leveling operations [10,11]. A leveling tool is commonly used to normalize surfaces prior to analysis, in different applications, to remove unwanted irregularities and roughness. Different leveling methods can be used for leveling mainly varying in the interpolation algorithms [12]. Leveling is used in a variety of scales and applications to facilitate the analysis of measurements. One example is trigonometric leveling in fluvial or coastal areas [13]. Erol [12] examined different interpolation algorithms in modeling the local geoid, an equipotential surface of the Earth's gravity field. A numerical test using surface leveling has shown that the calculated geoid model using the employed interpolation algorithm is an applicable alternative of the gravimetric geoid model in Turkey [12]. However, going back to the micro-scale surface topography, advanced characterization on micromorphology using appropriate filters was presented by da Conceição et al. [14] on the example of wood cutting surfaces measured with atomic force microscopy.

The surfaces of materials, both before operation and after destruction, say a lot about its potential durability and the possibility of distributing loads [15]. Especially fractography, a way in failure investigation for studying the fracture surface, can indicate a lot about the history of the material before its destruction [16–19]. Many external factors affecting damage, such as elevated temperature, are reflected in the topography of the fractures [20,21]. Advanced measurement methods, such as digital image correlation [22,23] and broadly understood microscopy [24–26] are particularly useful for quantitative fractography. In addition, the combination of modern research methods [27,28] with optical surface observation techniques [29,30] allow the development of alternative approaches to characterise the fracture surface, such as FRASTA (FRActure Surface Topography Analysis) method [31–33]. The aforementioned measurement tools also enable the



development of classical computational models and the search for non-standard methods, for instance the fractal dimension [34]. Recently, computer methods have also made it possible to develop cognitive processes of fatigue cracks mechanisms [35]. The same is true for surface metrology [36] and topography analyzes [37,38]. The advances in computing technology have enabled the development of sophisticated numerical simulation approaches to deal with classic problems based on the von Mises stress [39]. This made it possible to better evaluate together the strength and the stability of complex technical elements. An interesting example is related to analysis of adhesively bonded spar-wingskin joints made of fiber reinforced-polymer composite laminates and subjected to pull-off load. Based on an advanced three-dimensional finite element analysis, Rakshe et al [40] demonstrated that the material and spar thickness were the most significant factors influencing the von Mises stress.

This work aims at linking the fatigue behaviour of high-strength steels to the surface metrology features via the fractal dimension. This research is motivated by the need to develop a precise method for predicting fatigue life and crack initiation in engineering materials. To achieve this goal, it is proposed a new approach that combines the fractal dimension and other indicators into a single parameter, improving the overall accuracy concerning the prediction of crack initiation and total fatigue life. The paper alludes to related authors' work, either in terms of materials tested and loading scenarios [41–43] or in terms of the use of fractal dimension [44–47]. These works presented quite promising results, however in this article an optimal method based on the fractal dimension of fatigue fracture surface is developed. In addition, a new fatigue crack initiation model is presented based on both the applied loading and fracture surface topography. The model is successfully tested in steel subjected to bending-torsion fatigue, and it is expected to be applied to other materials and fatigue cases.

## 2. Experiments and numerical calculations

### 2.1. Materials and specimens

The materials under study, 34CrNiMo6 and 18Ni300 steel, are high-strength steels widely used in critical engineering components subjected to multiaxial loading [41]. The former was produced by conventional manufacturing and supplied in a quenched and tempered condition, while the latter was produced by selective laser melting. This selection is designed to test the proposed approach for different processing conditions in order to evaluate its overall sensitivity to the processing techniques. The micrographs of the 34CrNiMo6 and the 18Ni300 steels are shown in Fig. 1. The micrograph of the conventional 34CrNiMo6 steel (see Figure 1(a)) demonstrates a non-uniform distribution of precipitates. General, the material has a fine microstructure mainly composed of martensite and lower bainite. Martensite appears lighter while bainite appears darker. The average grain size, determined via the procedure outlined in ASTM E112, was equal to 8  $\mu\text{m}$ . Regarding the additively manufactured 18Ni300 steel, as showed in Figure 1(b), the microstructure is rather coherent, and is built by elongated grains, with about 150  $\mu\text{m}$  long and 30-35  $\mu\text{m}$  width. A corrugated region created by the melting in the first laser pass is also noticeable. Their chemical compositions are listed in Table 1 and Table 2, respectively. Figure 2 shows the shape and dimensions of the specimens tested in this research, namely a solid round bar with a lateral U-shaped notch made of 34CrNiMo6 steel (see Fig. 2(a)); a solid round bar with a blind hole plus U-shaped notch made of 34CrNiMo6 steel (Fig. 2(b)); and a hollow round bar with a transverse hole made of 18Ni300 steel (see Fig. 2(c)).

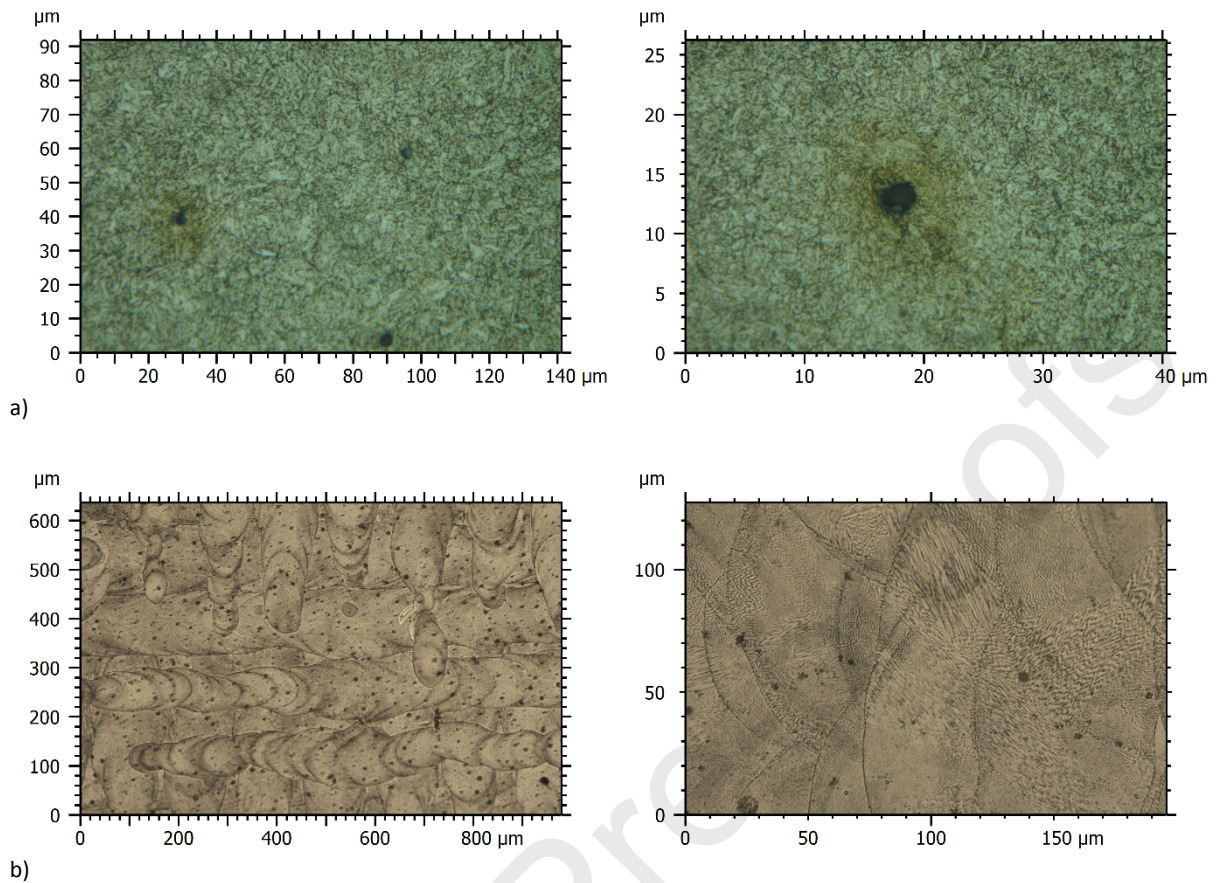


Fig. 1. Microstructure of the: (a) 34CrNiMo6 from a sample polished and etched with nital (mag.  $\times 1000$ ); and (b) 18Ni300 from a sample polished and etched with picral (mag.  $\times 100$  and  $\times 500$ ).

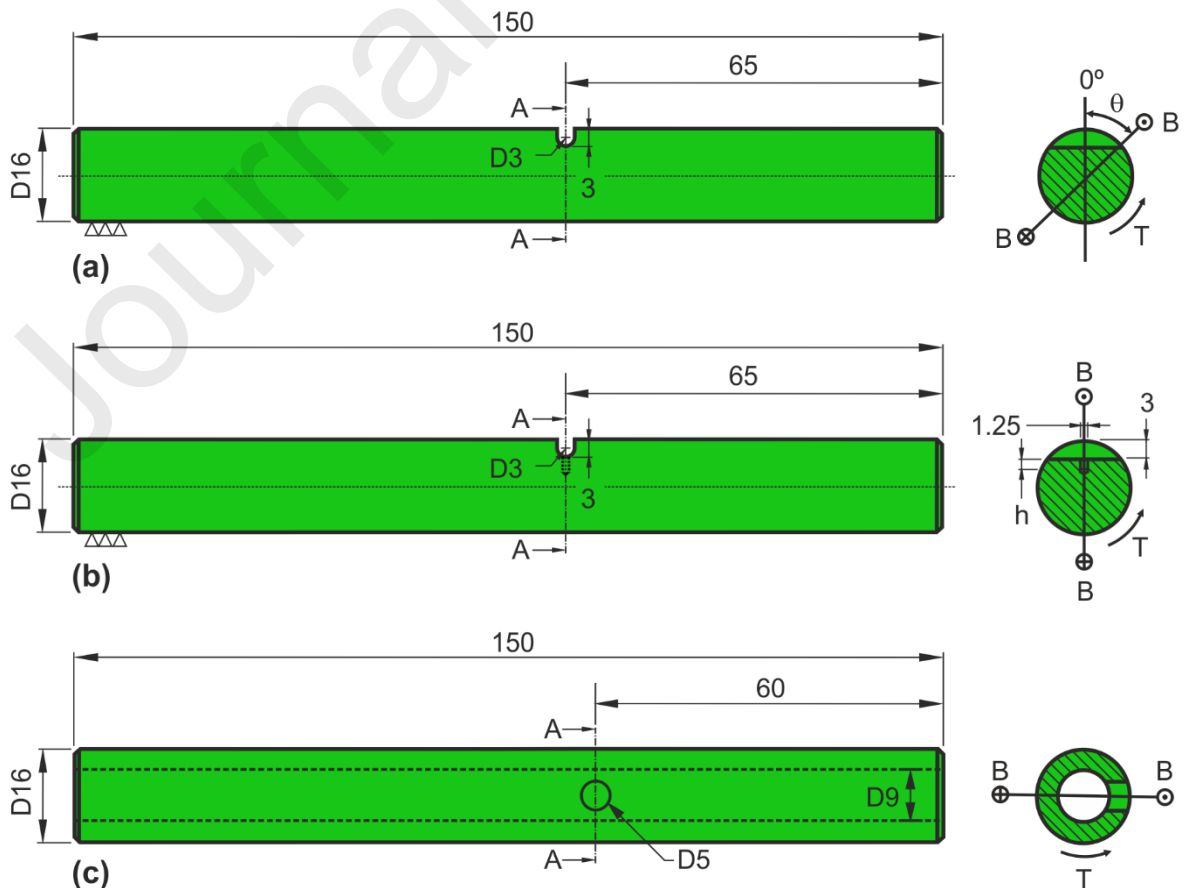


Fig. 2. Specimen geometries used in the experimental campaign: (a) solid round bar with lateral U-shaped notch 34CrNiMo6 for three bending orientations ( $\theta=0^\circ$ ,  $\theta=45^\circ$ , and  $\theta=90^\circ$ ); (b) solid round bar with transverse blind hole plus U-shaped notch (34CrNiMo6) with one bending orientation; and (c) hollow round bar with transverse hole (18Ni300) with one bending orientation. Dimensions in millimetres.

Table 1. Nominal chemical composition of 34CrNiMo6 (wt%).

| C    | Si          | Mn   | Cr   | Mo   | Ni   |
|------|-------------|------|------|------|------|
| 0.34 | $\leq 0.40$ | 0.65 | 1.50 | 0.22 | 1.50 |

Table 2. Nominal chemical composition of 18Ni300 (wt%).

| C    | Ni   | Mn   | Co  | Mo  | Ti  | Al   | Cr  | P    | Si  | Mn   | Fe      |
|------|------|------|-----|-----|-----|------|-----|------|-----|------|---------|
| 0.01 | 18.2 | 0.65 | 9.0 | 5.0 | 0.6 | 0.05 | 0.3 | 0.01 | 0.1 | 0.04 | Balance |

The three geometries were tested under proportional bending-torsion loading. Different bending moment to torsion moment ratios  $B/T$  were considered, namely  $B/T=2$ ,  $B/T=1$ , and  $B/T=2/3$ . These ratios corresponded to normal stress to shear stress ratios equal to  $\sigma/\tau=4$ ,  $\sigma/\tau=2$ , and  $\sigma/\tau=4/3$ . In the case of the geometry of Figure 2(a), the bending moment was applied for different orientations with respect to the notch root  $\theta$ , respectively  $\theta=0^\circ$ ,  $\theta=45^\circ$ , and  $\theta=90^\circ$  (see Figure 2(a)). In the other two cases, the bending moment was applied for  $\theta=0^\circ$  only. In the first case, it was considered three angles in order to test the ability of the proposed method to deal with different loading orientations. For each  $B/T$  ratio, different stress amplitudes were analysed. The applied stress amplitudes are listed in Table 3. All tests were performed under pulsating loading conditions, i.e.  $R=0$ . More details about the nominal stress amplitudes applied in the tests as well as the fatigue lives will be provided in Section 3.

## 2.2. Finite-element models

The stress fields at the notch region were evaluated numerically using three-dimensional finite element models. Figure 3 shows the typical models developed for the solid round bar with U-shaped notch made of 34CrNiMo6 high-strength steel (Figures 3a-c) and for the hollow round bar with transverse hole made of 18Ni300 maraging steel (Figures 3d-e). For the sake of simplicity, because the mesh of the solid round bar with transverse blind hole is rather similar to that of solid round bar with U-shaped notch is not displayed. In the three cases, the meshes were created in a parametric framework, with 8-node hexahedral elements, assuming a homogeneous, linear-elastic and isotropic behaviour. Around the geometric discontinuities, as can be seen in Fig. 3(b-c) and Fig. 3(e), ultra fine meshes were introduced in order to better characterise the stress gradients.

The assembled model of the: (1) solid round bar with lateral U-shaped notch had 76,608 elements and 99,823 nodes; (2) solid round bar with blind hole had 89,584 elements and 97,704 nodes; (3) and the hollow round bar with transverse hole had 152,248 elements and 163,138 nodes. Regarding the two first geometries, the loading scenarios were applied by four forces at one end while the other was fixed. The two  $F_B$  forces, with similar intensity, introduced the bending moment, while the two  $F_T$  forces, also with similar intensity, introduced the torsion moment. The bending moment to torsion moment ratios were defined via the  $\lambda$  parameter. As far as the third geometry, the loading cases were generated through a single force,  $F$ . The bending moment to torsion moment ratios were defined by changing the value of  $H$ , while the  $L$  distance was constant ( $H$  and  $L$  are identified in Fig. 3).



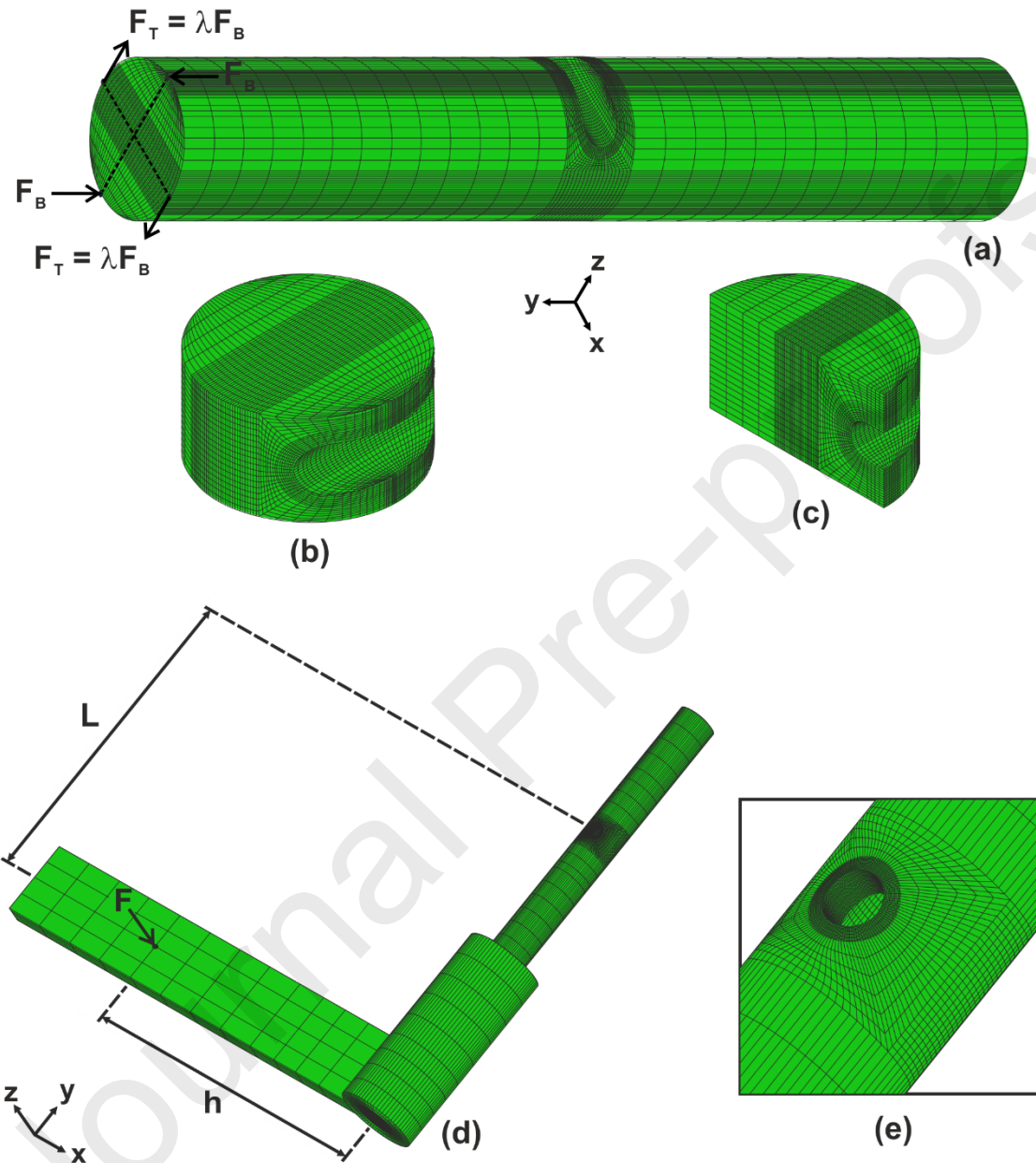


Fig. 3. Finite element models: (a,b,c) solid round bar with U-shaped notch (34CrNiMo6); (d,e) hollow round bar with transverse hole (18Ni300)

### 2.3. Surface topography measurement

Topographic measurements of the fracture surfaces were performed with an optical profilometer Alicona G4 using focus-variation technology with a  $\times 10$  lens [48,49]. Due to the restricted single field of view (FOV), 19 rows  $\times$  13 columns were stitched together to map the entire fracture area. This allowed to achieve an exemplary level for FOV of 14.817 mm  $\times$  15.926 mm, while

drastically increasing memory usage. Each individual micrograph had a vertical resolution 57.3 nm with a lateral resolution 3.91  $\mu\text{m}$  level. The whole surface was reduced to the region of interest (ROI) to eliminate the regions associated with the geometric discontinuities and to obtain uniform dimensions for all groups of specimens, as shown in Figure 4. Visualization of all extracted fracture surfaces, i.e. the region of interest (ROI) in the form of a grid views, and also the histograms and Abbott-Firestone curves are presented in Appendix A. The fracture surface maps were processed with the MountainsMap<sup>®</sup> software to quantitative analysis and visualization. The identity card for key details of data sets is presented in Appendix B. Additional measurements of the characteristic zones were made with 100 $\times$  magnification, and also by scanning electron microscopy (SEM). A similar configuration of equipment and software for surface analysis was used in the previous works [50,51].

The views of the fracture surfaces of the 20 tested specimens were carefully treated in order to extract the ROI. The method of selecting the ROI is shown in the Fig. 4 and is detailed described in the papers [41,52]. In summary, the original areas are reduced by eliminating the regions not related to the fracture surface. Figure 4 shows an example for each tested geometry of the original areas, on the left side, and the final areas, on the right side.

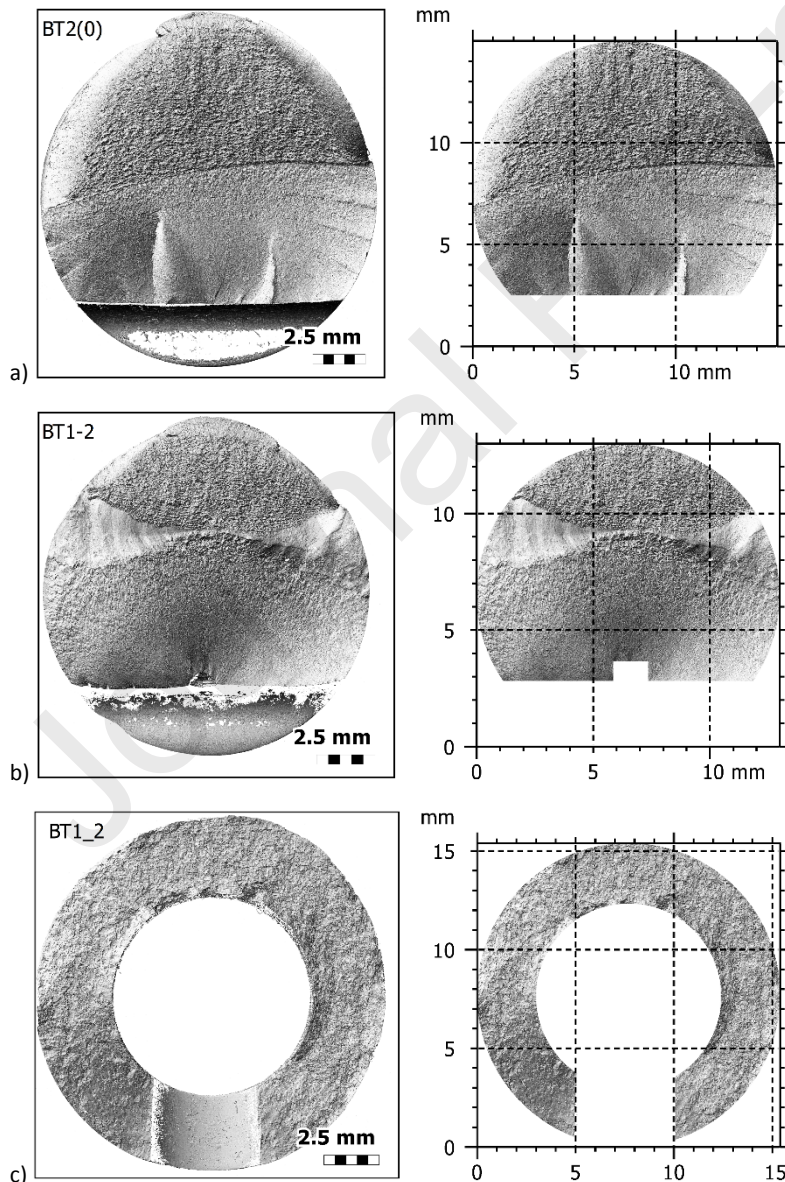


Fig. 4. Original and extracted fracture surfaces – ROI: (a) solid round bar with lateral U-shaped notch (34CrNiMo6); (b) solid round bar with transverse blind hole (34CrNiMo6); and (c) hollow round bar with transverse hole (18Ni300).

#### 2.4. Fractal dimension evaluation

The examined surfaces were analysed applying data leveling to eliminate the general plane slope [53,54]. The selected approach to carry out the leveling procedure was the least square plane method. It allows to minimize the quadratic deviations of a cloud of points representing a surface [55].

About fractal dimension  $D_f$ , when dividing the surface, algorithms have to maintain the number of iterations that take place. The resolution of the plot decides the number of iterations. In this analysis, for *coarse resolution*, it was 15 data points, and for *extra-fine resolution*, it was 96 data points. The enclosing boxes method (EBM) divides the area into smaller divisions with a width  $\varepsilon$  and calculates the field  $A\varepsilon$  of all fields covering the entire area. This is an iterative procedure where the width of the field is changed to plot, i.e.  $\ln(A\varepsilon)/\ln(\varepsilon)$ . To estimate the fractal dimension  $D_f$  a line is fitted using the least square method. The absolute value of the slope of the fitted line is the fractal dimension  $D_f$ . Fig. 5 shows exemplary plots of fractal dimension determined for *coarse resolution* (Fig. 5a) and *extra-fine resolution* (Fig. 5b). The curve is shown in green while the regression line is plotted in red. The resolution of the measurements has an impact on the results for calculation the fractal dimension  $D_f$  results because the densification of the measurement points increases the slope of the curve angle of the fractal dimension.

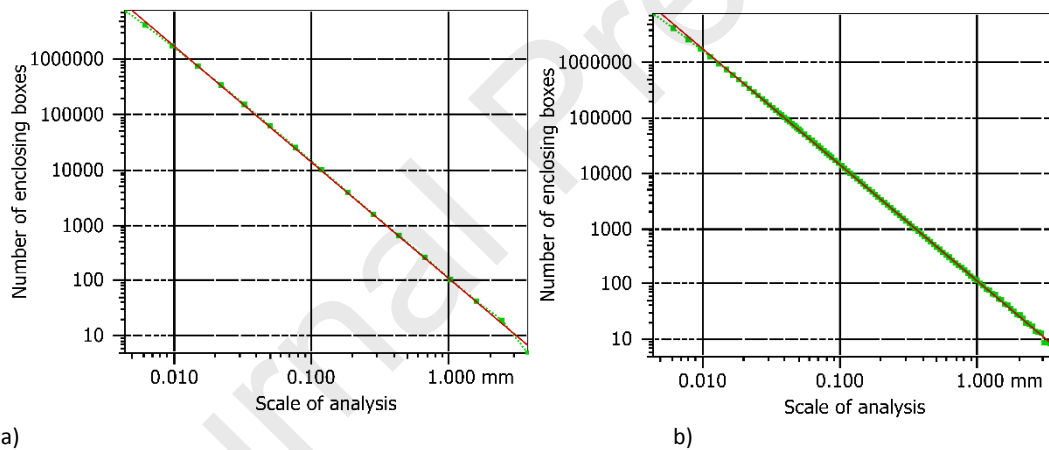


Fig. 5. Fractal analysis for the extracted area using the entire fracture surface method: (a) coarse resolution; and (b) extra-fine resolution.

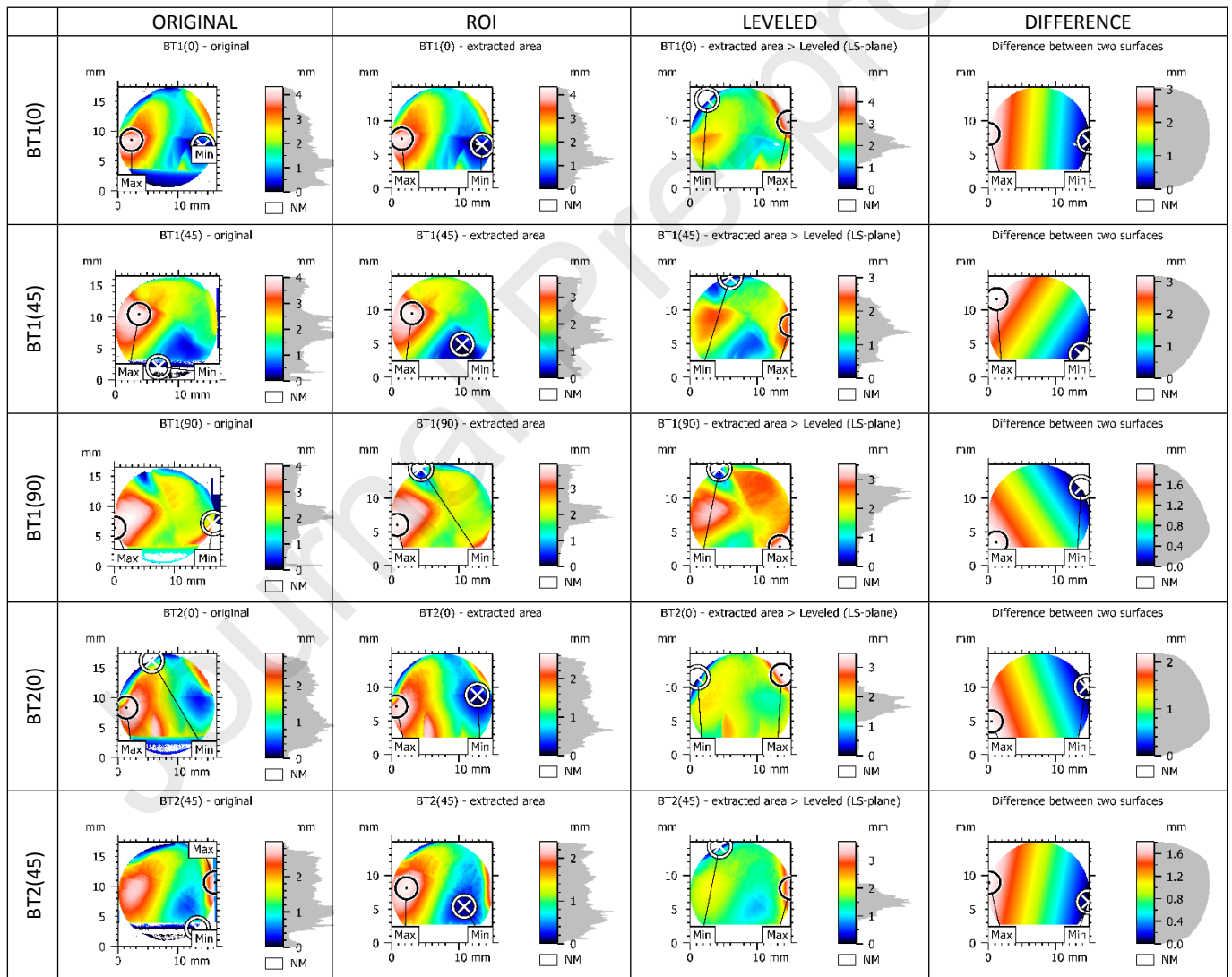
A comparison was also made for conventional surface topography parameters, namely using the root mean square height  $Sq$  (see Eq. (1)) and void volume  $V_v$  [56], according to ISO 25178 [57].

$$Sq = \sqrt{\frac{1}{A} \iint_A z^2(x,y) dx dy}, \quad (1)$$

where  $A$  is the definition area, and  $x$ ,  $y$ ,  $z$  are the relative coordinates of the Cartesian system with the  $z$ -axis defined in the height direction.

### 3. Results

The modus operandi of the studied surface, defined in the form of a  $z=f(x,y)$  transformation, consists of extracting the ROI from the original fracture surfaces. Next, the leveling procedure (LS-plane) is applied to the surface fracture. These tasks are presented in Figures 6-8 for the three tested geometries, i.e. the solid round bar with lateral U-shaped notch; the solid round bar with blind hole; and the hollow round bar with transverse blind hole, respectively. In the individual columns, looking from the left to the right, there are “ORIGINAL” surface, “ROI”, “LEVELED” plane, and “DIFFERENCE” between planes before and after leveling operation. The best fit least squares plane levelling operator is used to eliminate the slope of the surface. The before and after output of application of the levelling operator, i.e. ROI and LEVELED, are shown in Figures 6-8 (second and third columns, respectively). The lowest (Min) and highest (Max) points are displayed for each surface, as well as the color scale for  $z$  axis with a histogram. Leveling, inter alia, causes modifications in the surface geometry, such as changing the place of the lowest and highest points of the fracture planes. The first column of Figures 6-8 displays the specimen’s name as listed Table 3. This naming will be used throughout the remainder of the paper.



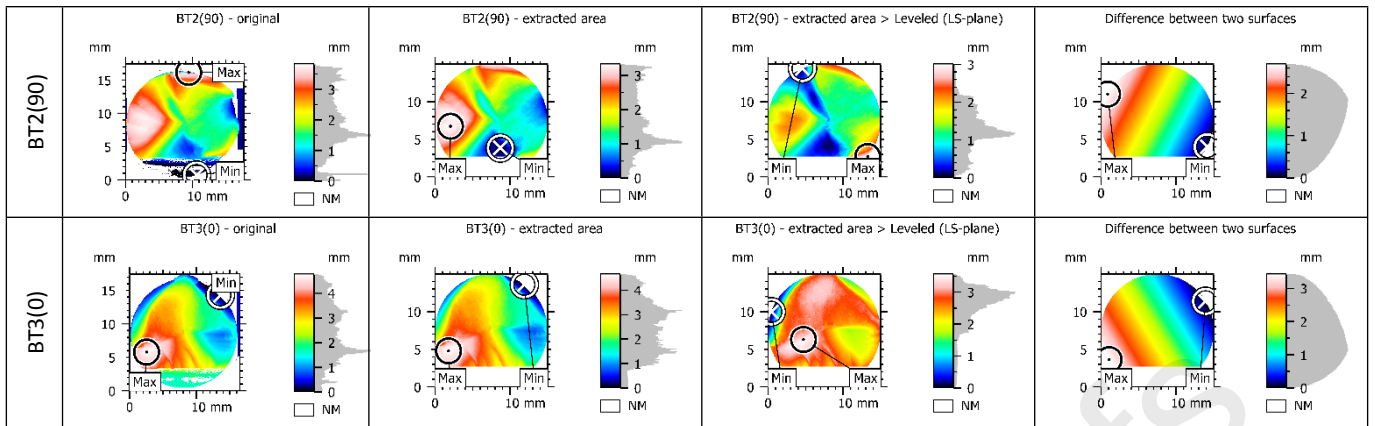


Fig. 6. Original surface, ROI, leveled plane, and difference between planes before and after leveling operation for the solid round bar with lateral U-shaped notch.

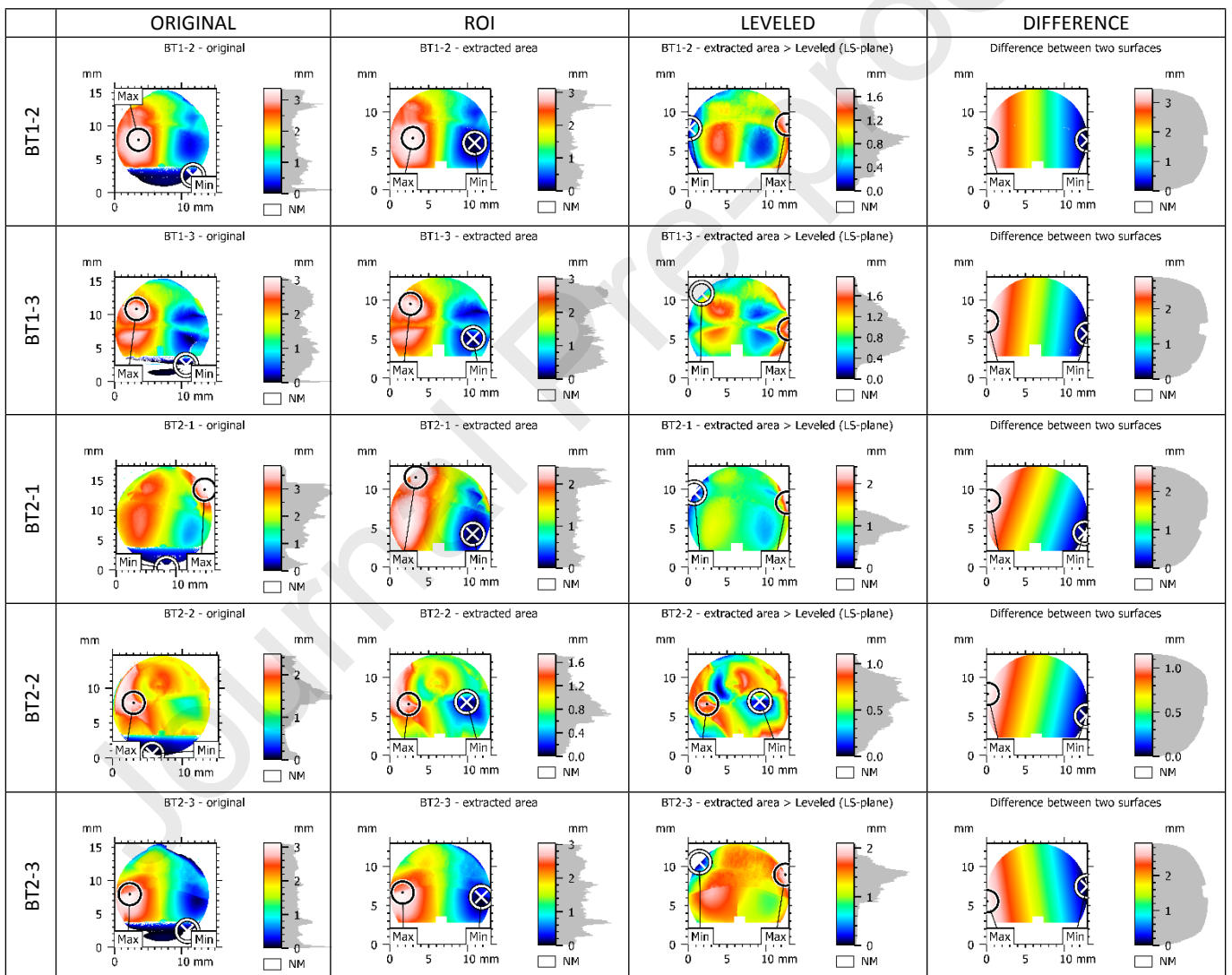


Fig. 7. Original surface, ROI, leveled plane, and difference between planes before and after leveling operation for the solid round bar with blind hole.

| ORIGINAL | ROI | LEVELED | DIFFERENCE |
|----------|-----|---------|------------|
|----------|-----|---------|------------|

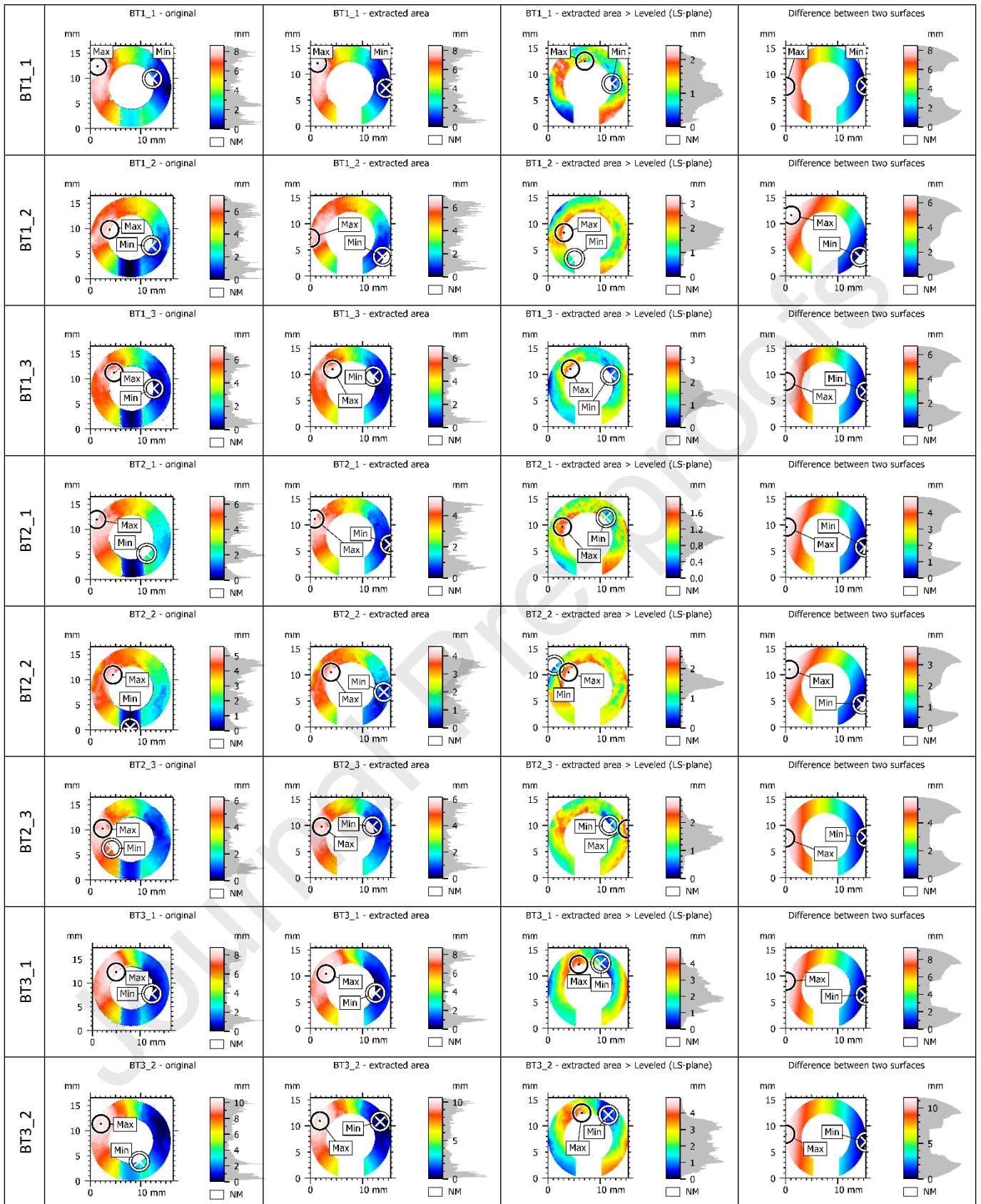


Fig. 8. Original surface, ROI, leveled plane, and difference between planes before and after leveling operation for the hollow round bar with transverse hole.

A summary of the multiaxial fatigue testing program and the maximum local equivalent von Mises stress  $\sigma_{VM}$  calculation results are presented in Table 3. The maximum stresses were calculated using the numerical models for the nodes at the notch region. Fatigue crack initiation life, represented by number of cycles to crack initiation  $N_i$ , was calculated for a crack length equal to the material characteristic length  $a_0$  [42], while the total failure was defined for a crack length equal to 4 mm. More details about the calculations of fatigue parameters give summary [42]. In turn, fractal dimension  $D_f$  results, depending on the resolution, are summarized in Table 4.

Table 3. Summary of the multiaxial fatigue testing program and maximum local equivalent von Mises stress  $\sigma_{VM}$ .

| Specimen                              | $B/T$ | $\sigma_a$<br>(MPa) | $\sigma_m$<br>(MPa) | $\sigma_{VM}$ (MPa) | $N_i$<br>(cycles) | $N_f$<br>(cycles) |
|---------------------------------------|-------|---------------------|---------------------|---------------------|-------------------|-------------------|
| 34CrNiMo6 high-strength steel (notch) |       |                     |                     |                     |                   |                   |
| BT1(0)                                | 1     | 179                 | 194                 | 610                 | 46,822            | 73,816            |
| BT1(45)                               | 1     | 209                 | 224                 | 676                 | 67,160            | 102,755           |
| BT1(90)                               | 1     | 284                 | 294                 | 641                 | 88655             | 119,383           |
| BT2(0)                                | 2     | 179                 | 194                 | 519                 | 49,103            | 70,758            |
| BT2(45)                               | 2     | 254                 | 269                 | 683                 | 39,331            | 56,769            |
| BT2(90)                               | 2     | 364                 | 379                 | 565                 | 51,878            | 71,591            |
| BT3(0)                                | 2/3   | 179                 | 189                 | 631                 | 50,261            | 82,010            |
| 34CrNiMo6 high-strength steel (hole)  |       |                     |                     |                     |                   |                   |
| BT1-2                                 | 1     | 179                 | 194                 | 1099                | 15,320            | 34,318            |
| BT1-3                                 | 1     | 298                 | 313                 | 1831                | 1,250             | 1,654             |
| BT2-1                                 | 2     | 224                 | 239                 | 1271                | 10,557            | 16,075            |
| BT2-2                                 | 2     | 179                 | 194                 | 1002                | 17,111            | 30,268            |
| BT2-3                                 | 2     | 179                 | 194                 | 1002                | 59,878            | 105,925           |
| 18Ni300 maraging steel                |       |                     |                     |                     |                   |                   |
| BT1_1                                 | 1     | 66                  | 73                  | 273                 | 79,878            | 123,126           |
| BT1_2                                 | 1     | 80                  | 88                  | 336                 | 48,564            | 70,405            |
| BT1_3                                 | 1     | 96                  | 105                 | 403                 | 15,000            | 21,030            |
| BT2_1                                 | 2     | 78                  | 86                  | 278                 | 81,000            | 205,261           |
| BT2_2                                 | 2     | 80                  | 88                  | 278                 | 140,000           | 280,233           |
| BT2_3                                 | 2     | 96                  | 105                 | 340                 | 45,500            | 82,943            |
| BT3_1                                 | 2/3   | 80                  | 88                  | 403                 | 22,000            | 49,550            |
| BT3_2                                 | 2/3   | 55                  | 61                  | 280                 | 110,000           | 144,803           |

$\sigma_a$ : nominal normal stress amplitude;  
 $\sigma_m$ : nominal normal mean stress;  
 $\sigma_{VM}$ : maximum local von Mises equivalent stress;  
 $N_i$ : number of cycles to crack initiation;  
 $N_f$ : number of cycles to failure.

Table 4. Fractal dimension  $D_f$  results.

| Specimen | Coarse   | Extra-fine | Leveling,<br>Coarse | Leveling,<br>Extra-fine |
|----------|----------|------------|---------------------|-------------------------|
| BT1(0)   | 2.106831 | 2.105872   | 2.116590            | 2.116259                |
| BT1(45)  | 2.119107 | 2.120130   | 2.137177            | 2.135776                |
| BT1(90)  | 2.108336 | 2.108048   | 2.116037            | 2.116391                |
| BT2(0)   | 2.129996 | 2.124020   | 2.144913            | 2.141041                |
| BT2(45)  | 2.153225 | 2.156719   | 2.169583            | 2.169773                |
| BT2(90)  | 2.115397 | 2.114458   | 2.130664            | 2.130298                |
| BT3(0)   | 2.113330 | 2.117949   | 2.134260            | 2.141858                |
| BT1-2    | 2.113724 | 2.119117   | 2.130724            | 2.141366                |

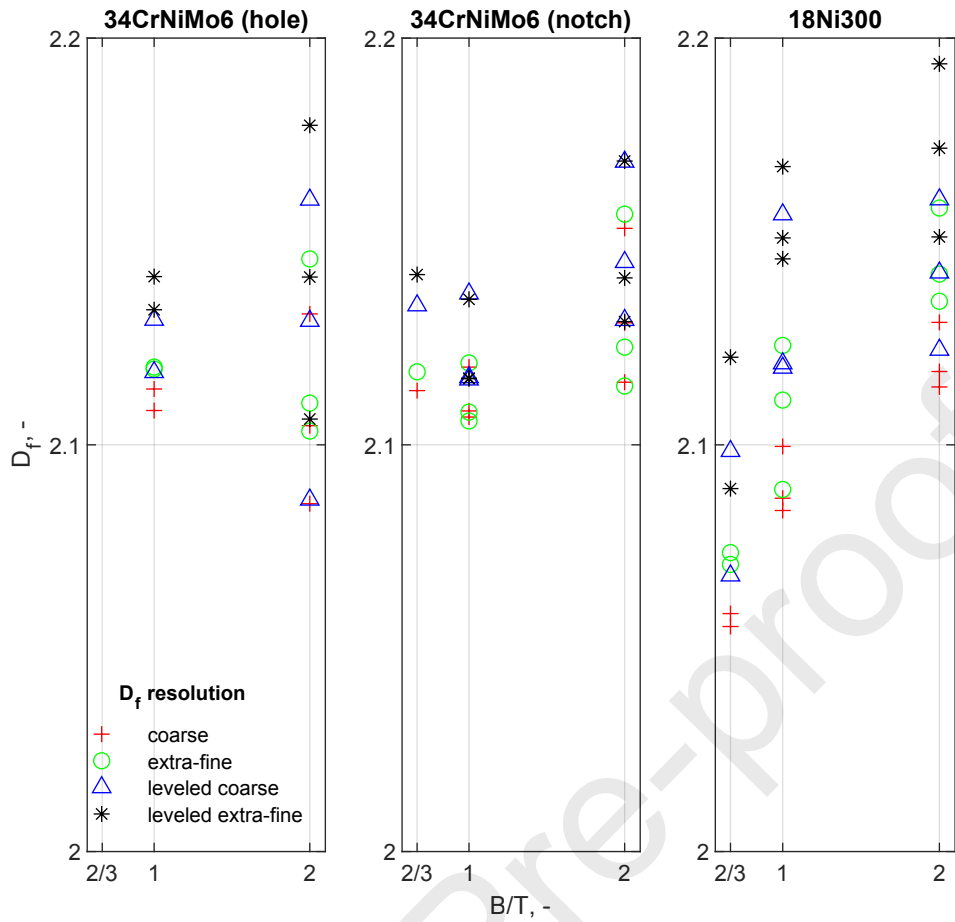
|       |          |          |          |          |
|-------|----------|----------|----------|----------|
| BT1-3 | 2.108438 | 2.118615 | 2.117847 | 2.133213 |
| BT2-1 | 2.132187 | 2.145701 | 2.160248 | 2.178562 |
| BT2-2 | 2.085518 | 2.103380 | 2.086497 | 2.106334 |
| BT2-3 | 2.104701 | 2.110260 | 2.130460 | 2.141251 |
| BT1_1 | 2.083854 | 2.089030 | 2.156636 | 2.168410 |
| BT1_2 | 2.086876 | 2.111002 | 2.118935 | 2.145716 |
| BT1_3 | 2.099609 | 2.124443 | 2.120006 | 2.150874 |
| BT2_1 | 2.118026 | 2.141978 | 2.160323 | 2.193679 |
| BT2_2 | 2.130106 | 2.158224 | 2.142334 | 2.172928 |
| BT2_3 | 2.114231 | 2.135292 | 2.123349 | 2.151113 |
| BT3_1 | 2.058505 | 2.073490 | 2.067848 | 2.089240 |
| BT3_2 | 2.055325 | 2.070593 | 2.098446 | 2.121532 |

#### 4. Discussion

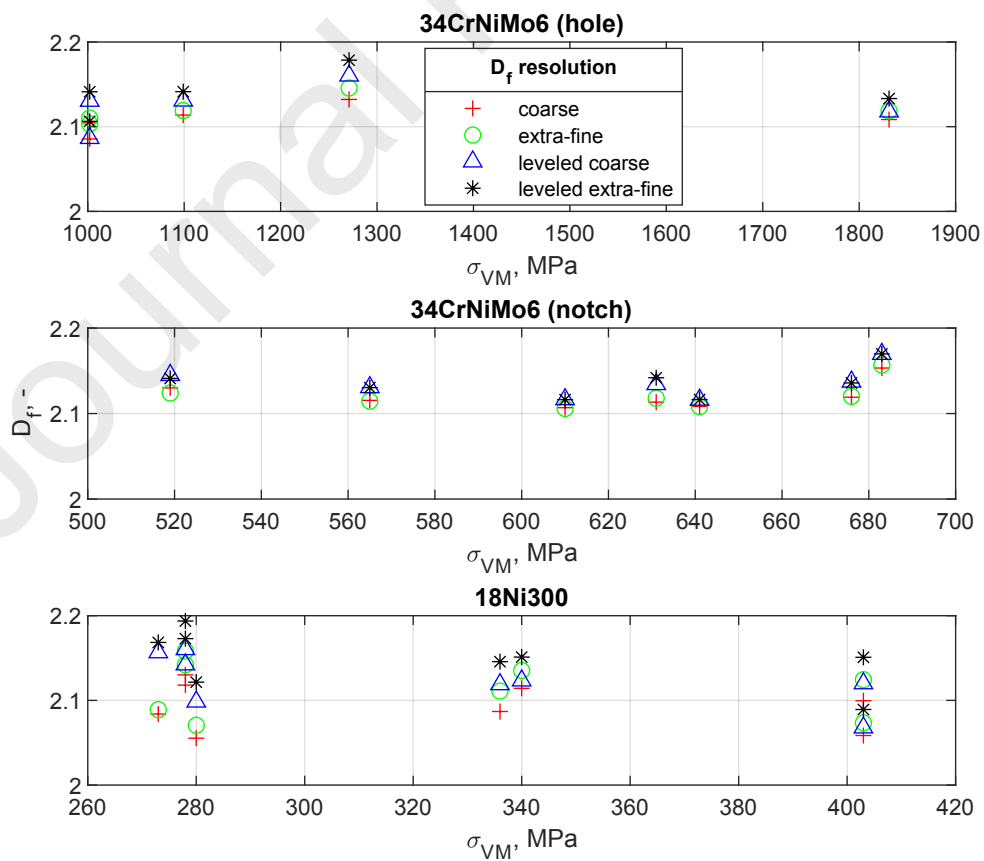
This section aims to analyse the relationship between the surface fractures and both the fatigue life and the fractal dimension  $D_f$ . The first sub-section is focused on the correlation between the fractal dimension and the fatigue variables; the second sub-section addresses the correlation between surface topography parameters and fatigue life; and the third sub-section deals with the fracture morphology features. Finally, the last sub-section presents the fatigue life predictions carried out through the proposed methodology.

##### 4.1. Correlation between fractal dimension and fatigue variables

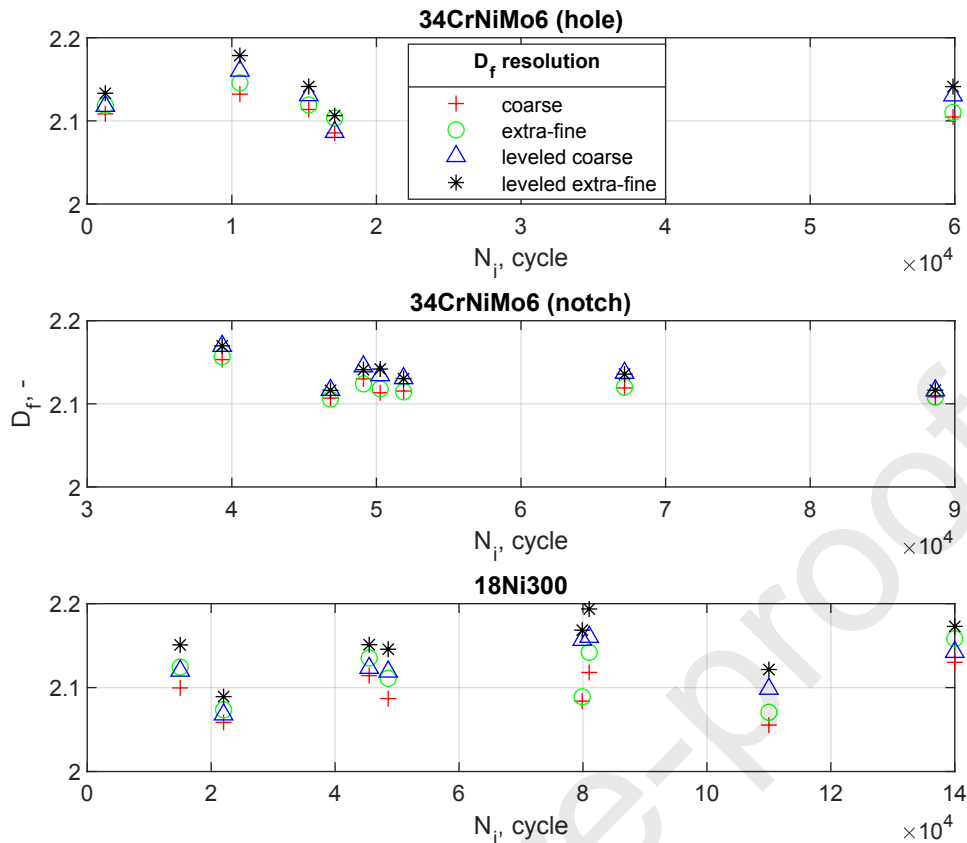
All results of fractal dimension  $D_f$  for the 20 investigated specimens obtained via the 4 considered options by the EBM are shown in Fig. 9. They were grouped by specimen type and are presented as follows: a)  $B/T$  ratio; b) maximum local equivalent von Mises stress  $\sigma_{VM}$ ; and c) number of cycles to crack initiation  $N_i$ .



a)



b)



c)

Fig. 9. Results of fracture surface fractal dimension  $D_f$  calculations grouped by specimens type versus: a)  $B/T$  ratio; b) maximum local von Mises equivalent stress  $\sigma_{VM}$ ; and c) number of cycles to crack initiation  $N_i$ .

As far as the value of the fractal dimension is concerned, the  $D_f$  relationship was maintained for all calculated parameters and, in general, both leveling and higher  $f_r$  resolution increased the value of the fractal dimension. All the samples had a relatively small scatter of values between the calculation methods, the differences in the  $D_f$  values varied from 2.055 to 2.194 (see table 4). Moreover, the two extreme values of the fractal dimension  $D_f$  were achieved for the 18Ni300 specimens, more specifically the lowest was obtained for BT3\_2 with *coarse resolution*, while the highest was obtained for leveled BT2\_1 with *extra-fine resolution*.

The fitted functions, as well as the correlation coefficients, for all fractal dimension  $D_f$  calculation cases considered in this research are compiled in Tables 5-7. They are organized as follows:  $B/T$  ratio, maximum local equivalent von Mises stress  $\sigma_{VM}$ , and number of cycles to crack initiation  $N_i$ . These functions allow to better identify the most suitable method for determining the fractal dimension from a perspective of fatigue response.

Table 5. Fitted fractal dimension  $D_f$  versus  $B/T$  ratio.

| $D_f$ resolution   | 34CrNiMo6 (hole)           | $R^2$   | 34CrNiMo6 (notch)         | $R^2$ | 18Ni300                   | $R^2$ |
|--------------------|----------------------------|---------|---------------------------|-------|---------------------------|-------|
| coarse             | $D_f = -0.0361 B/T + 2.11$ | 0.0139  | $D_f = 0.0184 B/T + 2.10$ | 0.449 | $D_f = 0.0420 B/T + 2.04$ | 0.857 |
| extra-fine         | $D_f = 0.00091 B/T + 2.12$ | 0.00097 | $D_f = 0.0158 B/T + 2.10$ | 0.302 | $D_f = 0.0487 B/T + 2.05$ | 0.809 |
| leveled coarse     | $D_f = 0.00145 B/T + 2.12$ | 0.00089 | $D_f = 0.0185 B/T + 2.11$ | 0.357 | $D_f = 0.0324 B/T + 2.08$ | 0.407 |
| leveled extra-fine | $D_f = 0.00476 B/T + 2.13$ | 0.0102  | $D_f = 0.015 B/T + 2.12$  | 0.234 | $D_f = 0.0391 B/T + 2.10$ | 0.533 |

$D_f$ : Fractal dimension (dimensionless)  
 $B/T$ : bending-to-torsion ratio (dimensionless)

Table 6. Fitted functions of surface topography versus maximum local von Mises equivalent stress  $\sigma_{VM}$ .

| $D_f$ resolution   | 34CrNiMo6 (hole)                                | $R^2$  | 34CrNiMo6 (notch)                               | $R^2$  | 18Ni300                               | $R^2$  |
|--------------------|---|--------|---|--------|---------------------------------------|--------|
| coarse             | $D_f = 1.31 \times 10^{-5} \sigma_{VM} + 2.09$  | 0.0734 | $D_f = 5.31 \times 10^{-5} \sigma_{VM} + 2.09$  | 0.0376 | $D_f = -0.00012 \sigma_{VM} + 2.13$   | 0.063  |
| extra-fine         | $D_f = 1.32 \times 10^{-5} \sigma_{VM} + 2.1$   | 0.0815 | $D_f = 0.0001 \sigma_{VM} + 2.06$               | 0.122  | $D_f = -0.000102 \sigma_{VM} + 2.15$  | 0.0303 |
| leveled coarse     | $D_f = 8.11 \times 10^{-6} \sigma_{VM} + 2.115$ | 0.0112 | $D_f = 6.32 \times 10^{-5} \sigma_{VM} + 2.097$ | 0.4156 | $D_f = -0.000364 \sigma_{VM} + 2.241$ | 0.4365 |
| leveled extra-fine | $D_f = 9.73 \times 10^{-6} \sigma_{VM} + 2.13$  | 0.0172 | $D_f = 8.44 \times 10^{-5} \sigma_{VM} + 2.08$  | 0.0743 | $D_f = -0.000347 \sigma_{VM} + 2.26$  | 0.358  |

$\sigma_{VM}$ : maximum local equivalent von Mises stress (MPa)

Table 7. Fitted functions of surface topography versus number of cycles to crack initiation  $N_i$ .

| $D_f$ resolution   | 34CrNiMo6 (hole)                        | $R^2$   | 34CrNiMo6 (notch)                       | $R^2$ | 18Ni300                                | $R^2$  |
|--------------------|---|---------|---|-------|--|--------|
| coarse             | $D_f = -1.62 \times 10^{-7} N_i + 2.11$ | 0.0479  | $D_f = -5.07 \times 10^{-7} N_i + 2.15$ | 0.269 | $D_f = 1.67 \times 10^{-7} N_i + 2.08$ | 0.699  |
| extra-fine         | $D_f = -2.68 \times 10^{-7} N_i + 2.12$ | 0.143   | $D_f = -5.25 \times 10^{-7} N_i + 2.15$ | 0.262 | $D_f = 1.77 \times 10^{-7} N_i + 2.10$ | 0.0551 |
| leveled coarse     | $D_f = 5 \times 10^{-8} N_i + 2.12$     | 0.00181 | $D_f = -6.36 \times 10^{-7} N_i + 2.17$ | 0.331 | $D_f = 3.07 \times 10^{-7} N_i + 2.10$ | 0.188  |
| leveled extra-fine | $D_f = -4.7 \times 10^{-8} N_i + 2.14$  | 0.0017  | $D_f = -6.48 \times 10^{-7} N_i + 2.17$ | 0.345 | $D_f = 3.10 \times 10^{-7} N_i + 2.13$ | 0.172  |

$N_i$ : number of cycles to crack initiation (cycles)

Based on the data, the fractal dimension  $D_f$  is less dependent on the  $B/T$  ratio than other selected surface topography parameters [41], reaching a low coefficient of determination  $R^2$ , at least in terms of linear dependence. The exception is the 18Ni300 steel, for which  $R^2$  equals 0.857. Therefore, in order to relate the fractal dimension  $D_f$  with other materials and fatigue parameters, it would be necessary to use matches in a function other than linear.

Figure 10 shows interactive linear fitting curves between resolutions. Conversely, Table 8 indicates fitting model parameters for  $D_f$  calculation resolutions. For all fits, prediction bounds with confidence levels of 90% were added. Prediction bounds establish the lower and upper values of the associated interval and define the width of the interval. The width of the interval reflects the level

of uncertain of the fitted coefficients, the predicted observations, or the predicted fits. In this study, as referred to above, the bounds were defined with a level of certainty of 90%. This means that there is a 10% chance that a new observation may be not correct. This interval indicates 90% chance that the fractal dimension measurement result is expected to fall within the lower and upper prediction bounds.

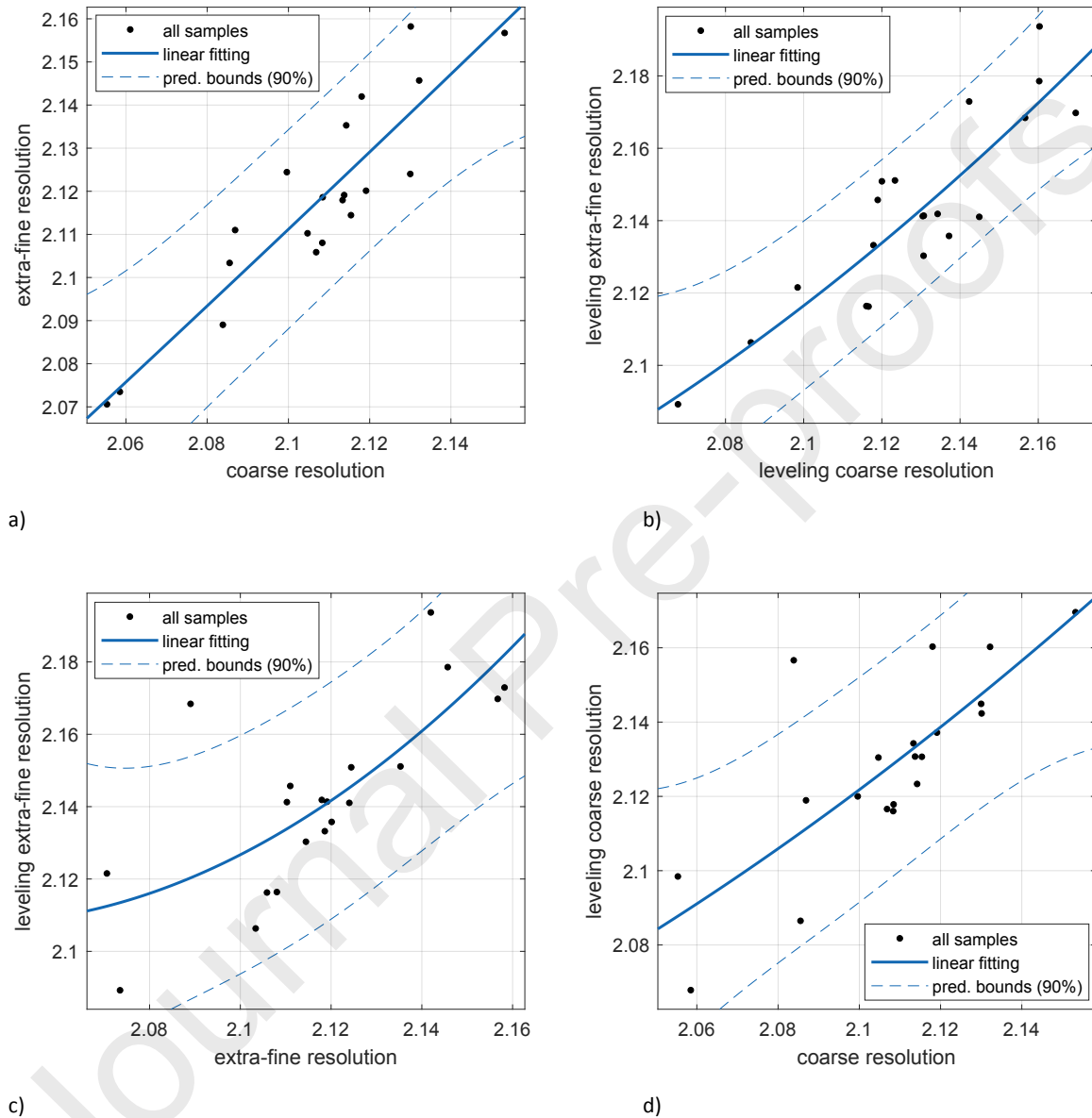


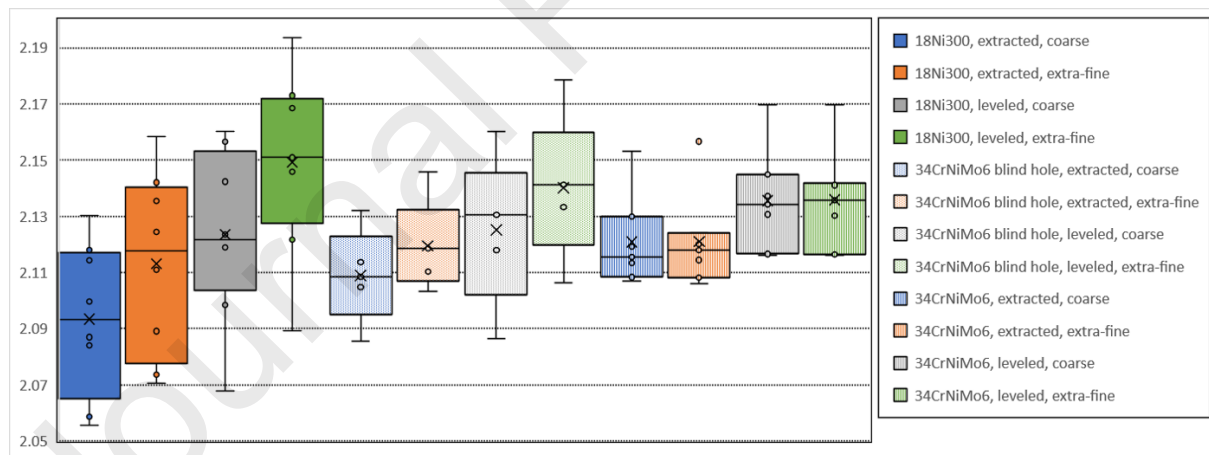
Fig. 10. Interactive linear fitting curves between resolutions: a) extra-fine versus coarse; b) levelling extra-fine versus levelling coarse; c) levelling extra-fine versus extra-fine; and d) levelling coarse versus coarse.

Table 8. Fitting model parameters for  $D_f$  calculation resolutions.

| Linear model: $f(x) = a \times (\sin(x-\pi)) + b \times ((x-10)^2) + c$ |                       |   |                                     |                             |
|---|-----------------------|---|-------------------------------------|-----------------------------|
|   | extra-fine vs. coarse | levelling extra-fine vs. levelling coarse | levelling extra-fine vs. extra-fine | levelling coarse vs. coarse |
| coefficients  | a = 0.4902            | a = 3.805                                 | a = 11.62                           | a = 2.827                   |
|   | b = -0.04083          | b = 0.06888                               | b = 0.3306                          | b = 0.03854                 |
|   | c = 5.083             | c = 1.102                                 | c = -8.478                          | c = 2.157                   |
| goodness of fit   | SSE: 0.001878         | SSE: 0.002746                             | SSE: 0.005604                       | SSE: 0.004757               |
|   | $R^2$ : 0.8209        | $R^2$ : 0.783                             | $R^2$ : 0.5571                      | $R^2$ : 0.6045              |
|   | RMSE: 0.01051         | RMSE: 0.01271                             | RMSE: 0.01816                       | RMSE: 0.01673               |

The best fit is shown by extra-fine versus coarse case (see Fig. 10(a)) with  $R^2 = 0.8209$  while the worst is levelling extra-fine versus extra-fine (see Fig. 10(c)) with  $R^2 = 0.5571$ . The results of extra-fine versus coarse and levelling extra-fine versus levelling coarse take a 10% chance that a new observation may be not correct. Plots from Figs. 10(c) and 10(d) are outside the 90% interval.

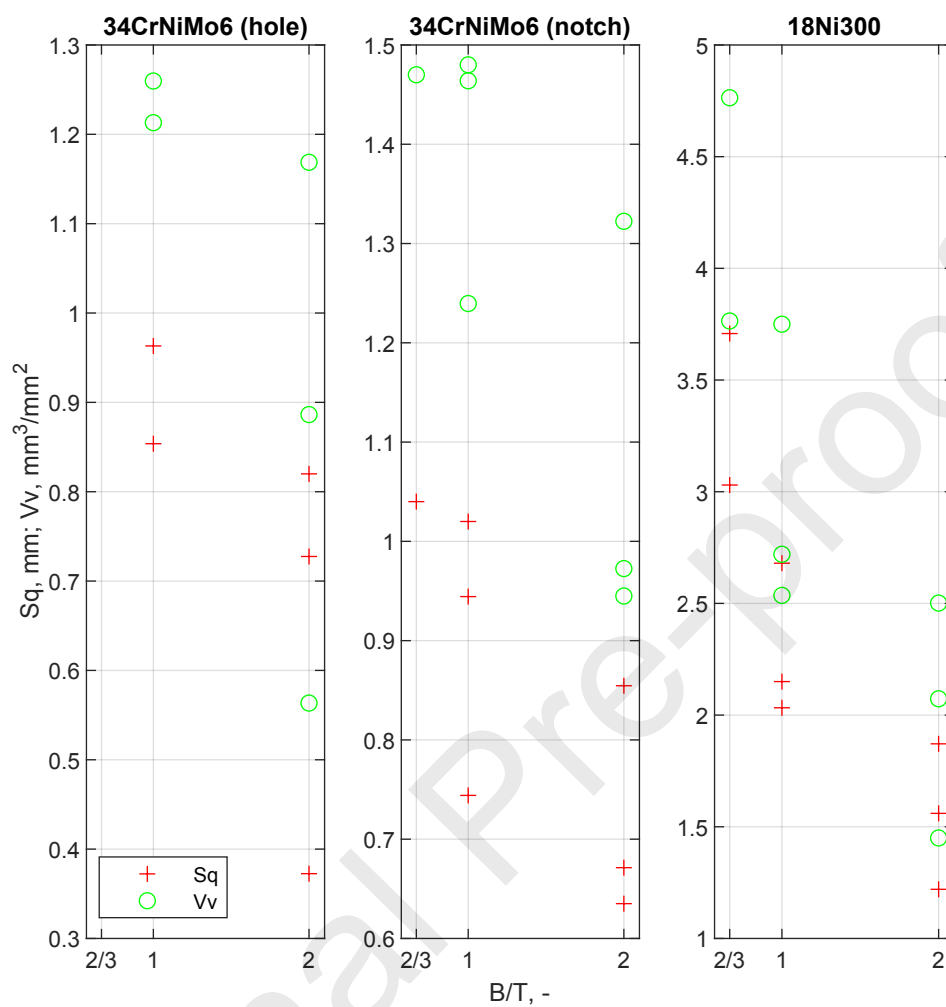
Fig. 11 shows boxplots for average fractal dimension  $D_f$  values grouped by the calculation methods. As can be seen, when averaging, both the leveling and the higher resolution increase the value of fractal dimension  $D_f$ . The densification of the measurement points increases the slope of the curve angle, which is reflected in a slightly higher value of the fractal dimension  $D_f$ .

Fig. 11. BOXPLOTS FOR FRACTAL DIMENSION  $D_f$  GROUPED BY EBM CALCULATIONS PARAMETERS.

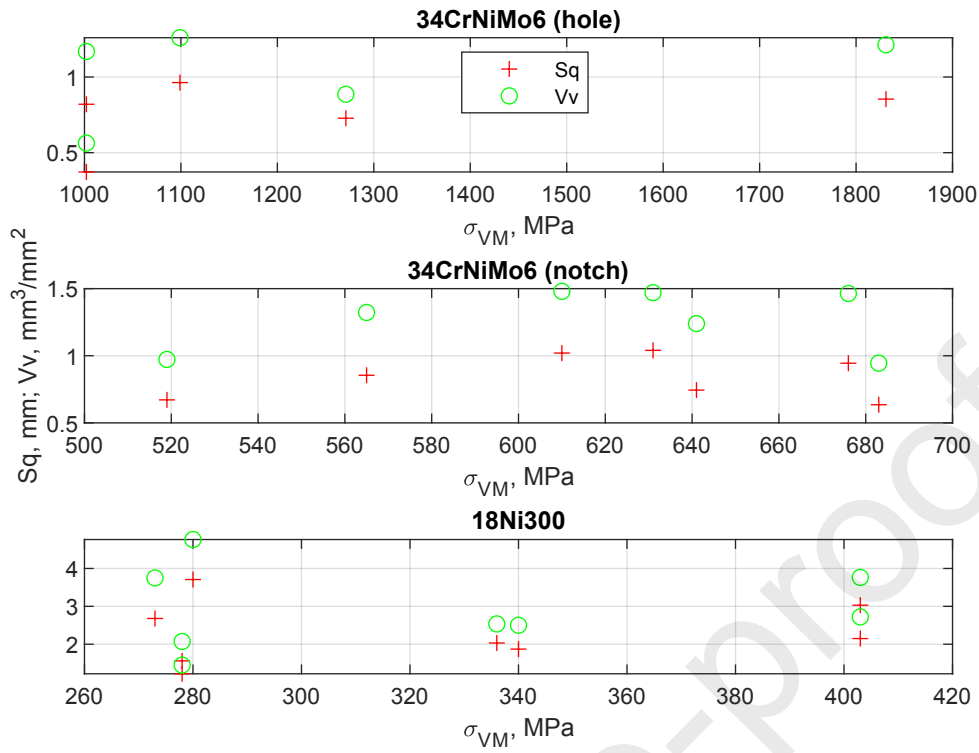
#### 4.2. Correlation between conventional surface topography parameters and fatigue results

In this section, for comparison, the surface topography parameters  $S_q$  and  $V_v$  [57], previously selected as the best fit parameters [41,56], are used. In addition, for comparison purposes, non-leveled surfaces were also analyzed, in order to examine if the leveling process affects the accuracy or distorts the results for surface geometries generated under bending-torsion loading. All the results of the surface topography parameters  $S_q$  and  $V_v$  for the 20 investigated specimens are exhibited in Fig. 12. They were grouped by specimen type and are presented as follows: a)  $B/T$  ratio; b) maximum local equivalent von Mises stress  $\sigma_{VM}$ ; and c) number of cycles to crack initiation  $N_f$ . Fitted surface

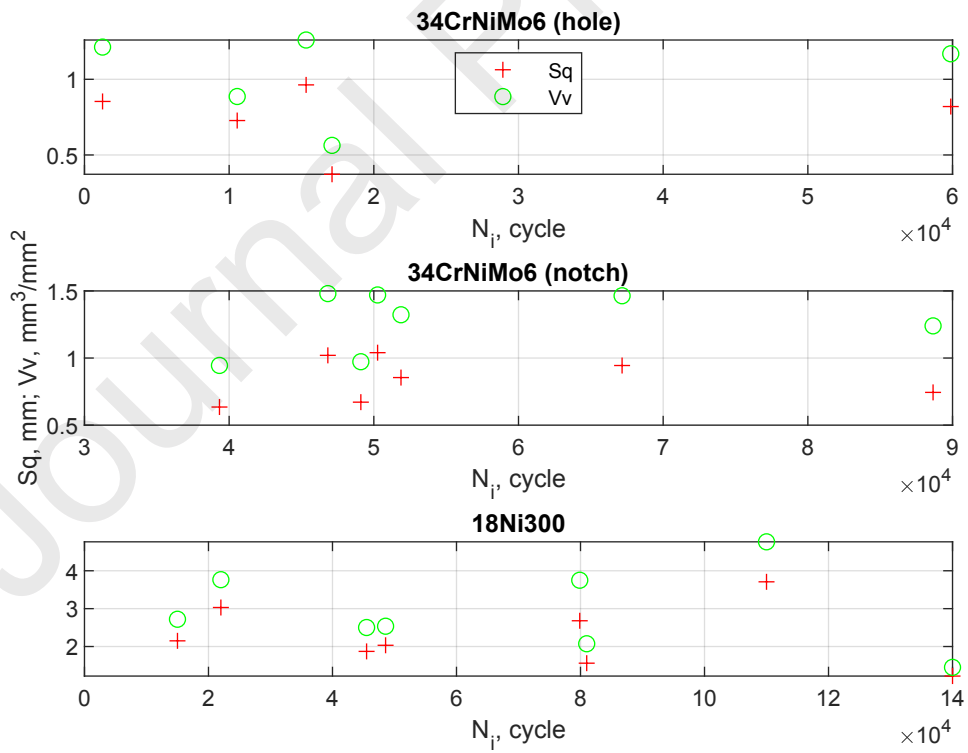
topography parameters  $Sq$  versus  $B/T$  ratio and  $Vv$  versus  $B/T$  ratio obtained via linear functions are presented in Table 9.



a)



b)



c)

Fig. 12. Results of fracture surface topography parameters  $Sq$  and  $Vv$  versus: a)  $B/T$  ratio; b) maximum local von Mises equivalent stress  $\sigma_{VM}$ ; and c) number of cycles to crack initiation  $N_i$ .

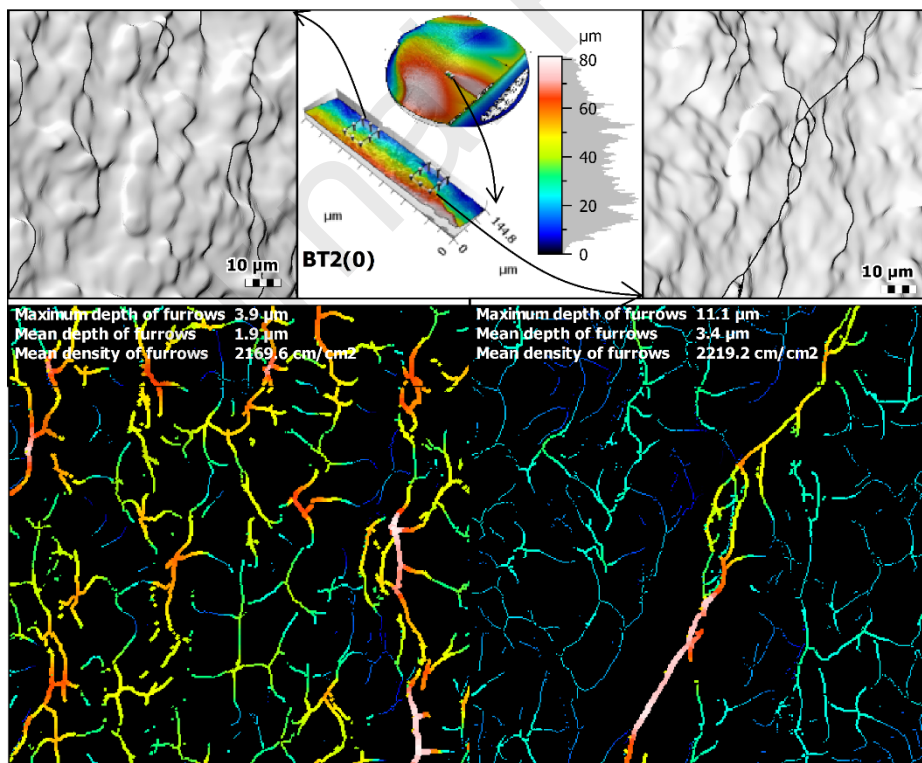
Table 9. Fitted surface topography parameters  $Sq$  versus  $B/T$  ratio and  $Vv$  versus  $B/T$  ratio.

| Surface topography | 34CrNiMo6 (hole)<br>$R^2$ | 34CrNiMo6 (notch)<br>$R^2$ | 18Ni300<br>$R^2$ |
|--------------------|---------------------------|----------------------------|------------------|
| $Sq$               | 0.424                     | 0.559                      | 0.721            |
| $Vv$               | 0.462                     | 0.608                      | 0.666            |

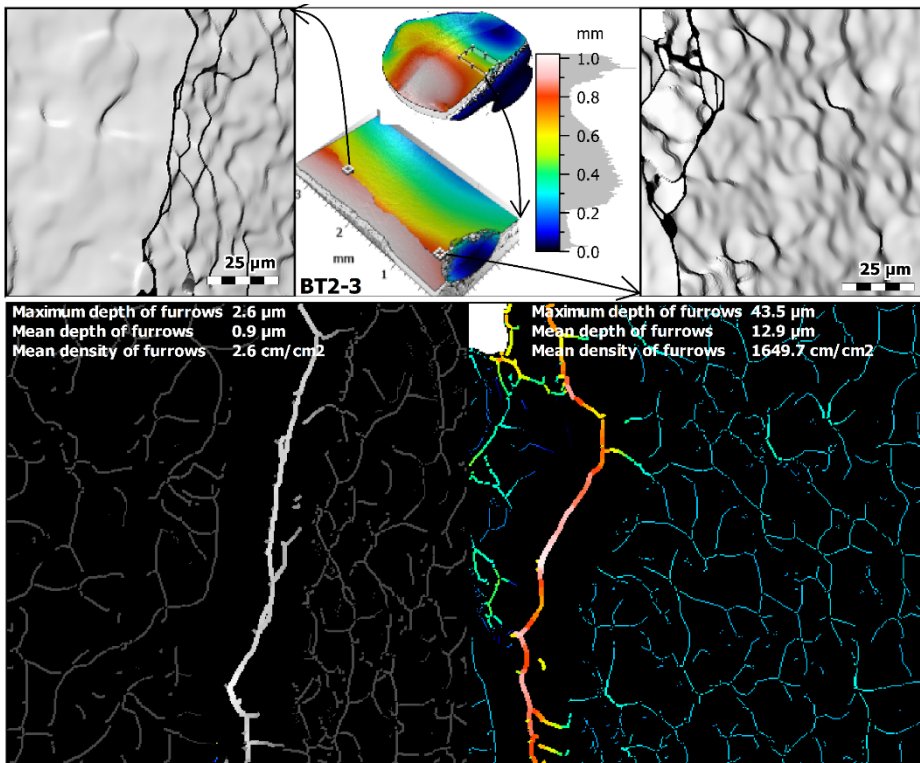
Both  $Sq$  and  $Vv$  parameters show, in general, low correlation coefficients for the linear function for all types of samples. The highest accuracy is shown by the  $Sq$  parameter for the hollow round bars made of 18Ni300 steel, and the lowest also by the  $Sq$  parameter for the solid round bar with blind hole made of 34CrNiMo6 steel. Thus, it would be recommended a function other than linear.

#### 4.3. Fracture morphology analysis

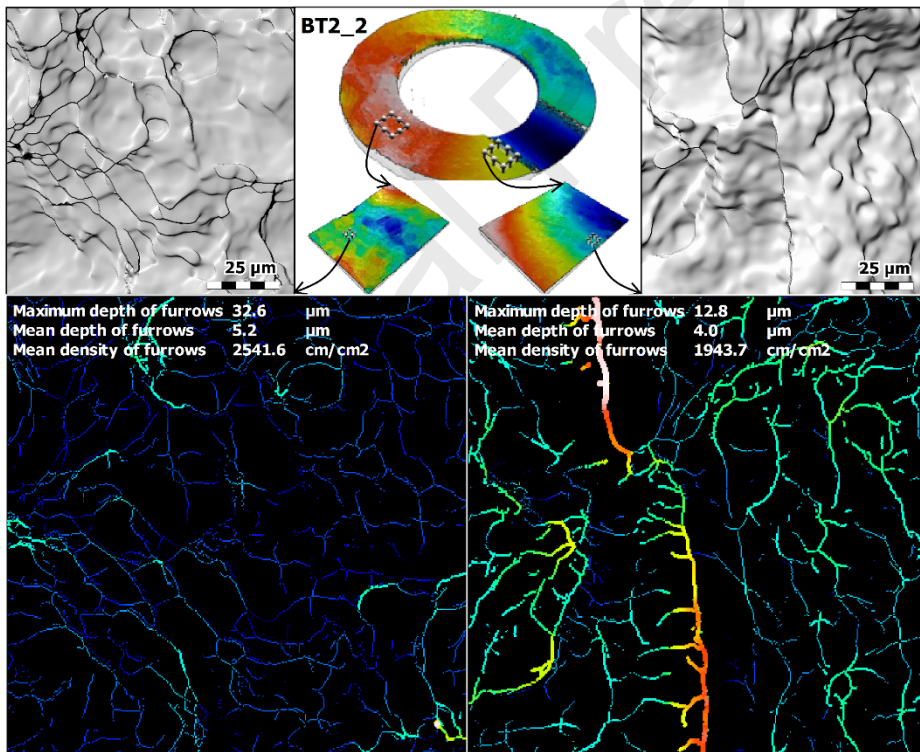
When we are investigating the shape of the fracture surface, it is useful to use various measurement methods because it allows to obtain complete information about the fracture formation. In this perspective, the analysis of surface morphologies was complemented by measuring furrows and by SEM observation. Graphical representations of the furrows for characteristic zones and SEM figures of initiation sites are displayed in Figs. 13 and 14, respectively. Furrow renderings (see Fig. 13) are obtained through Fourier transform applied by MountainsMap on topographic height functions that simulate furrows about peaks and valleys along the surface for better qualitative visualization of the fracture surface morphology.



a)



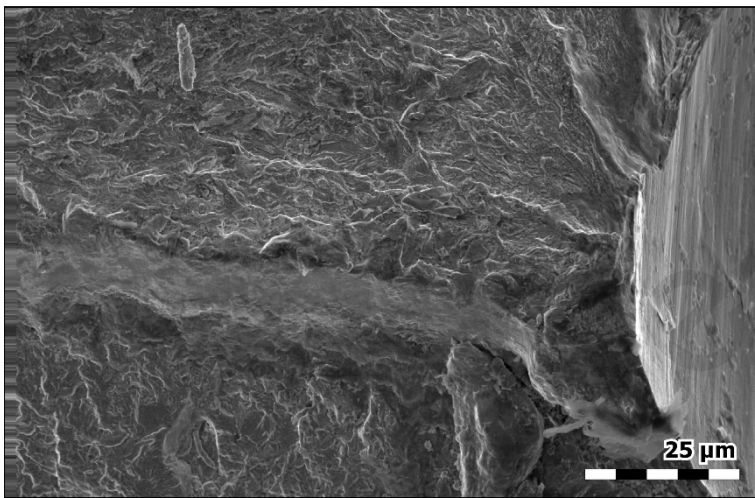
b)



c)

Fig. 13. Graphical representations of the furrows for characteristic zones, for specimens: (a) solid round bar with lateral U-shaped notch (34CrNiMo6: BT2(0)); (b) solid round bar with lateral U-shaped notch and with transverse blind hole (34CrNiMo6: BT2-3); and (c) hollow round bar with transverse hole (18Ni300: BT\_2).

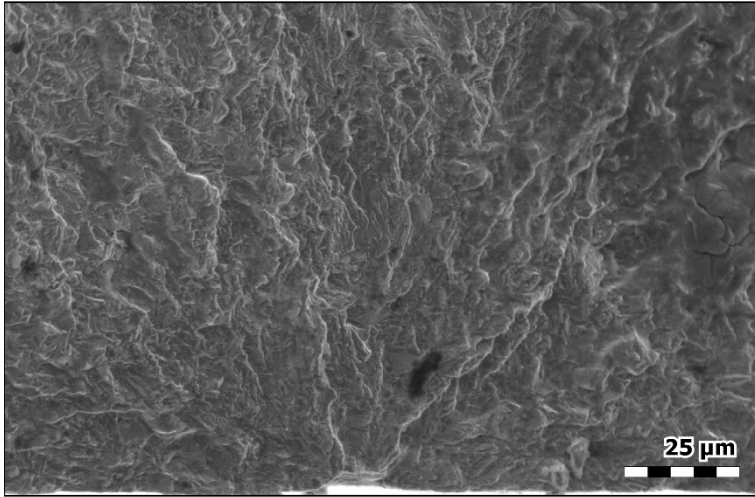
The regions on the right-side images (initiation zones) have furrows deeper and less spread. This translates into greater maximum depth furrows, which in turn is due to microcracks on the ROI. On the other hand, propagation regions with less intense but more aggregated structures have much lower values of maximum depth furrows. The case of the hollow round bar with transverse hole (18Ni300, BT\_2) deviates from this as for the values of the furrow parameters. It was observed that the sample BT2\_2 has a greater presence of evenly distributed channels (lines with less intense colors) as well as lesser interaction between the valleys. This showed that the rupture zones are rougher than the initiation zones, in which the distribution of the particles on the surface is interfered. The texture distribution of the initiation and propagation regions was similar for all cases observed in terms of furrow parameters, but there were deeper single furrows in the initiation zones. SEM micrographs (see Fig. 16) also give symptoms about the morphology of the fracture surface.



a)



b)



c)

Fig. 14. SEM images of the fracture morphology near crack initiation site: (a) solid round bar with lateral U-shaped notch (34CrNiMo6); (b) solid round bar with lateral U-shaped notch and with transverse blind hole (34CrNiMo6); and (c) hollow round bar with transverse hole (18Ni300).

#### 4.4. Prediction of number of cycles to crack initiation

The results presented in Section 4.2 showed that both the  $Sq$  and  $Vv$  parameters do not show satisfactory consistency as a linear function for all types of samples. Therefore, at a further stage of the research, we used combinations of the most suitable surface topography parameters in combination with, for example, the number of cycles to crack initiation  $N_i$  in order to develop a model capable to estimate the fatigue lifetime.

The crack initiation model applied in this research is based on the most suitable topography parameters identified in previous works [45], i.e.  $Sq$  and  $Vv$ , fractal dimension  $D_f$  (extra-fine) as well as on the maximum local equivalent von Mises stress  $\sigma_{VM}$ . In this approach, a new parameter  $P$ , defined in Eq. (2), was introduced:

$$P = \frac{\sigma_{VM} \times D_f}{Sq/Vv} \quad (2)$$

where  $\sigma_{VM}$  is the maximum local equivalent von Mises stress,  $D_f$  is the fractal dimension,  $Sq$  is the root mean square height, and  $Vv$  is the void volume. Fig. 15 shows the correlation between the new parameter  $P$  and the number of cycles to crack initiation  $N_i$  for all tested cases. Overall, as can be seen, the proposed parameter is sensitive to the fatigue crack initiation life. As can be seen, the results can be fitted by power functions with a high correlation coefficient, which is an interesting outcome.

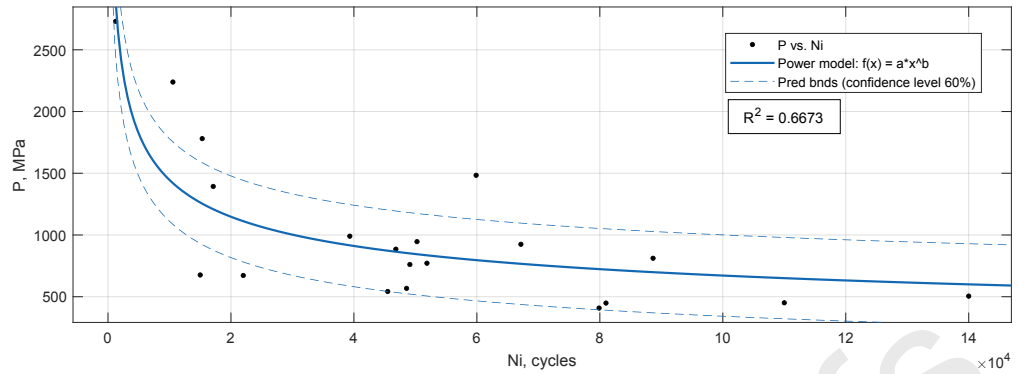


Fig. 15. Topographic stress factor  $P$  versus number of cycles to crack initiation  $N_i$  with a power fit.

The observed number of cycles to crack initiation  $N_i$  and the predicted number of cycles to crack initiation  $N_{ical}$  computed from the fracture surface parameter model (see Eq. (3)) is compared in Fig. 16. As can be seen, the calculations correlated well with the experimental results, regardless of the material and the specimen geometry.

$$N_{ical} = 6.514 \times 10^6 \times P^{-0.6733} - 21090 \quad (3)$$

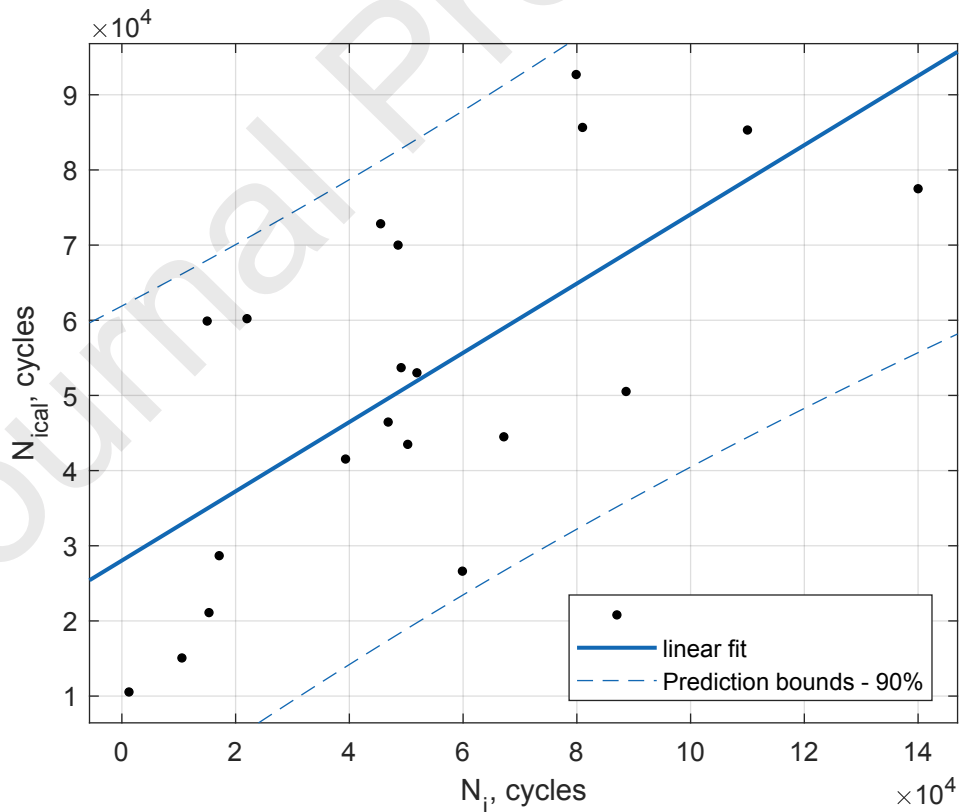


Fig. 16. Comparison of the predicted  $N_{ical}$  and the observed number of cycles to crack initiation  $N_i$ .

The total fatigue life  $N_f$  and the number of cycles to crack initiation  $N_i$  are key information for fatigue failure. To compare these parameters, Fig. 17 shows the plots of the total fatigue life  $N_f$  versus number of cycles to crack initiation  $N_i$ , depending on the loading ratio  $B/T$  for the analysed fatigue fractures. Based on these data, it is possible to compare  $N_i$  with  $N_f$  for different loading conditions. Although the loading conditions and the individual lives are different, the values of the  $N_i/N_f$  ratio are very similar. Thus, the parameter  $P$  can also be successfully used to estimate the fatigue life  $N_f$ .

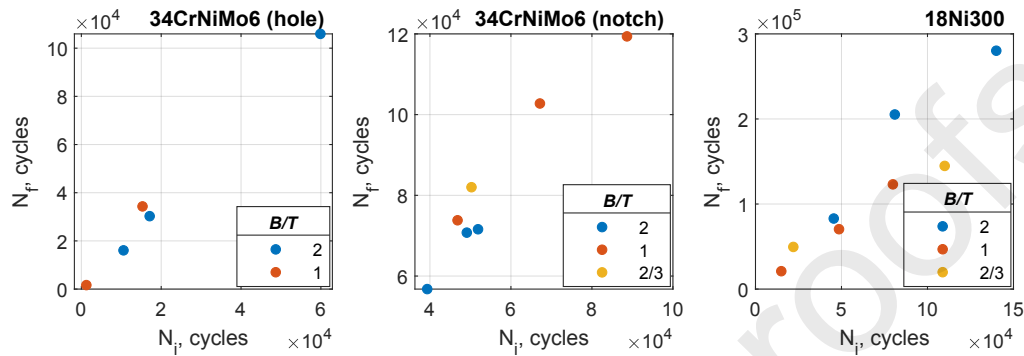


Fig. 17. Total fatigue life  $N_f$  vs. number of cycles to crack initiation  $N_i$  depending on loading ratio  $B/T$  for selected fatigue fractures.

## 5. Conclusions

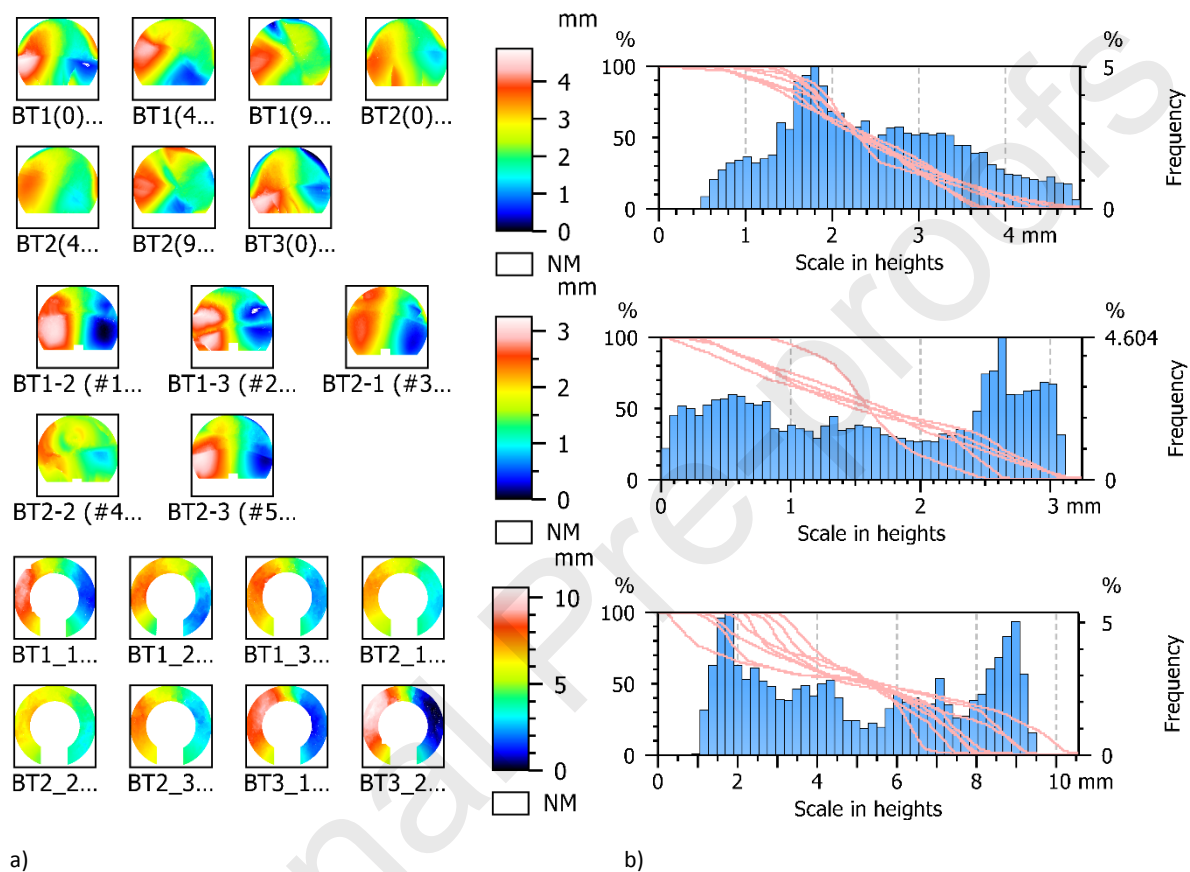
Metrological filters have a great influence on the parameters of surface topography. Therefore, it is important to select them correctly, especially in the case of a plane slope for fatigue fractures, where additional damage information is hidden in the slope. Based on the present study, the following conclusions can be drawn:

- From the point of view of fracture mechanics, the optimal calculation option for the fractal dimension  $D_f$  using the enclosing boxes method (EBM) is extra-fine resolution without leveling;
- The cracking mechanisms are directly associated with the fatigue crack direction which means that fracture surface slopes should be kept for analysis using higher resolutions to achieve the greater accuracy measurements;
- Conventional surface topography parameters  $Sq$  and  $Vv$  can satisfactorily correlate with the bending moment to torsion moment ratio  $B/T$  via linear functions for all the tested materials and specimen geometries;
- The topographic stress factor  $P$  exhibited a good correlation with the number of cycles to crack initiation  $N_i$  for the different loading cases tested in this research, regardless of the tested material and specimen geometry.

The entire fracture surface method is an easy-to-use tool which can be applicable to a wide range of technical problems related to failure analysis, including different engineering materials, geometrical configurations and loading histories. In reference to surface metrology, the method is universal and can be performed using different standard and non-standard surface parameters. This issue is very important because it connects the fracture mechanics with surface metrology allowing a deeper understanding of the failure mechanisms.

## Appendix A. Grid views and histogram &amp; Abbott-Firestone curve of the extracted area

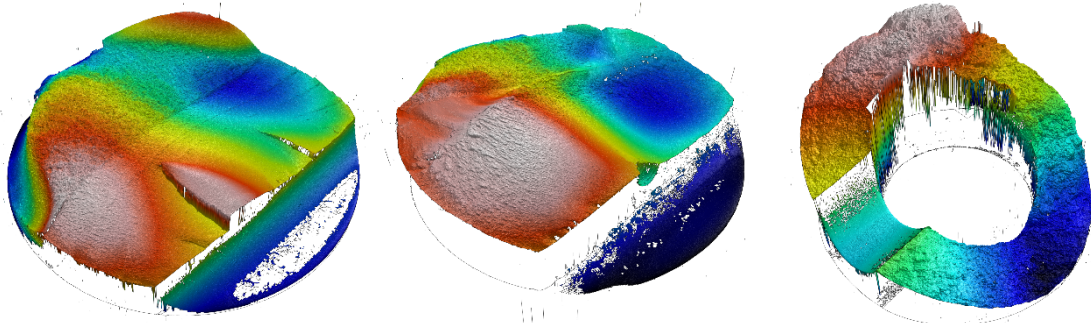
Simultaneous display of all extracted area for analysed fractures surfaces composing in thumbnail images is presented in Figure A1 (a). In Fig. A1 (b) is plot a histogram allowing to observe the height distribution with drawn Firestone curves, which are cumulating function of the depth distribution. Respectively, these are ROIs for: solid round bar with lateral U-shaped notch (34CrNiMo6); solid round bar with lateral U-shaped notch and with transverse blind hole (34CrNiMo6); and hollow round bar with transverse hole (18Ni300).



a) b) Figure A1. ROIs in the form of a grid view with histogram & Abbott-Firestone curves.

## Appendix B. Key details of data sets

The data sets (as a point clouds) were processed in MountainsMap surface analysis software through the production of topography gradient maps. Figure B1 presents general information about studiable, generated after transfer to the software, depending on the data supported by the AL3D file format. The topography gradient maps corresponding to original surfaces are shown at the top of Figure B1.



| Identity card - BT2(0) |            |        |  | Identity card - BT1-2 |            |        |  | Identity card - BT1_1 |            |        |  |
|------------------------|------------|--------|--|-----------------------|------------|--------|--|-----------------------|------------|--------|--|
| <b>Axis:</b>           | <b>X</b>   |        |  | <b>Axis:</b>          | <b>X</b>   |        |  | <b>Axis:</b>          | <b>X</b>   |        |  |
| Length:                | 16.479     | mm     |  | Length:               | 15.224     | mm     |  | Length:               | 16.478     | mm     |  |
| Size:                  | 18712      | points |  | Size:                 | 17287      | points |  | Size:                 | 18711      | points |  |
| Spacing:               | 0.881      | µm     |  | Spacing:              | 0.881      | µm     |  | Spacing:              | 0.881      | µm     |  |
| Offset:                | 0.000      | mm     |  | Offset:               | 0.000      | mm     |  | Offset:               | 0.000      | mm     |  |
| <b>Axis:</b>           | <b>Y</b>   |        |  | <b>Axis:</b>          | <b>Y</b>   |        |  | <b>Axis:</b>          | <b>Y</b>   |        |  |
| Length:                | 17.446     | mm     |  | Length:               | 15.622     | mm     |  | Length:               | 16.528     | mm     |  |
| Size:                  | 19809      | points |  | Size:                 | 17738      | points |  | Size:                 | 18767      | points |  |
| Spacing:               | 0.881      | µm     |  | Spacing:              | 0.881      | µm     |  | Spacing:              | 0.881      | µm     |  |
| Offset:                | -17.446    | mm     |  | Offset:               | -15.622    | mm     |  | Offset:               | -16.528    | mm     |  |
| <b>Axis:</b>           | <b>Z</b>   |        |  | <b>Axis:</b>          | <b>Z</b>   |        |  | <b>Axis:</b>          | <b>Z</b>   |        |  |
| Channel type:          | Topography |        |  | Channel type:         | Topography |        |  | Channel type:         | Topography |        |  |
| Length:                | 2.892      | mm     |  | Length:               | 3.364      | mm     |  | Length:               | 8.603      | mm     |  |
| Min:                   | -0.007     | mm     |  | Min:                  | -0.005     | mm     |  | Min:                  | -0.027     | mm     |  |
| Max:                   | 2.885      | mm     |  | Max:                  | 3.358      | mm     |  | Max:                  | 8.576      | mm     |  |
| Size:                  | 2891827    | digits |  | Size:                 | 3363831    | digits |  | Size:                 | 8603333    | digits |  |
| Spacing:               | 0.001      | µm     |  | Spacing:              | 0.001      | µm     |  | Spacing:              | 0.001      | µm     |  |

a)

b)

c)

Figure B1. Identity cards for measured data files (AL3D): (a) solid round bar with lateral U-shaped notch (34CrNiMo6); (b) solid round bar with lateral U-shaped notch and with transverse blind hole (34CrNiMo6); and (c) hollow round bar with transverse hole (18Ni300).

## References

- [1] M. Wu, W. Wang, D. Shi, Z. Song, M. Li, Y. Luo, Improved box-counting methods to directly estimate the fractal dimension of a rough surface, *Measurement*. 177 (2021) 109303. <https://doi.org/10.1016/J.MEASUREMENT.2021.109303>.
- [2] T. Ai, R. Zhang, H.W. Zhou, J.L. Pei, Box-counting methods to directly estimate the fractal dimension of a rock surface, *Applied Surface Science*. 314 (2014) 610–621. <https://doi.org/10.1016/J.APSUSC.2014.06.152>.
- [3] P.M. Silva, J.B. Florindo, A statistical descriptor for texture images based on the box counting fractal dimension, *Physica A: Statistical Mechanics and Its Applications*. 528 (2019) 121469. <https://doi.org/10.1016/J.PHYSA.2019.121469>.
- [4] M.A. Taylor, W.P. Bowen, Quantum metrology and its application in biology, *Physics Reports*. 615 (2016) 1–59. <https://doi.org/10.1016/J.PHYSREP.2015.12.002>.
- [5] R. Taymanov, K. Sapozhnikova, Metrological self-check and evolution of metrology, *Measurement*. 43 (2010) 869–877. <https://doi.org/10.1016/J.MEASUREMENT.2010.04.004>.
- [6] R.M. Reddy, B.N. Rao, Stochastic fracture mechanics by fractal finite element method, *Computer Methods in Applied Mechanics and Engineering*. 198 (2008) 459–474. <https://doi.org/10.1016/J.CMA.2008.08.014>.

- [7] S. Cui, J. Fu, S. Cen, H.R. Thomas, C. Li, The correlation between statistical descriptors of heterogeneous materials, *Computer Methods in Applied Mechanics and Engineering*. 384 (2021) 113948. <https://doi.org/10.1016/J.CMA.2021.113948>.
- [8] ISO 3274:1996(en), Geometrical Product Specifications (GPS) — Surface texture: Profile method — Nominal characteristics of contact (stylus) instruments, (n.d.). <https://www.iso.org/obp/ui/#iso:std:iso:3274:ed-2:v1:en> (accessed December 14, 2021).
- [9] ISO - ISO 16610-21:2011 - Geometrical product specifications (GPS) — Filtration — Part 21: Linear profile filters: Gaussian filters, (n.d.). <https://www.iso.org/standard/50176.html> (accessed August 21, 2021).
- [10] P. Podulka, W. Macek, R. Branco, R.M. Nejad, Reduction in Errors in Roughness Evaluation with an Accurate Definition of the S-L Surface, *Materials* 2023, Vol. 16, Page 1865. 16 (2023) 1865. <https://doi.org/10.3390/MA16051865>.
- [11] M. Bartoszek, Approximately Model of the Maximum Temperature on the Chip Surface, *Materials* 2021, Vol. 14, Page 2592. 14 (2021) 2592. <https://doi.org/10.3390/MA14102592>.
- [12] S. Erol, B. Erol, A comparative assessment of different interpolation algorithms for prediction of GNSS/levelling geoid surface using scattered control data, *Measurement*. 173 (2021) 108623. <https://doi.org/10.1016/J.MEASUREMENT.2020.108623>.
- [13] G. Bitelli, G. Roncari, M.A. Tini, L. Vittuari, High-precision topographical methodology for determining height differences when crossing impassable areas, *Measurement*. 118 (2018) 147–155. <https://doi.org/10.1016/J.MEASUREMENT.2018.01.013>.
- [14] W.S. da Conceição, R.S. Matos, L. Bufalino, G.Q. Ramos, F.G. Zayas, H.D. da Fonseca Filho, Micromorphology and fractal evaluation of Dinizia excelsa Ducke wood under three different cut conditions by atomic force microscopy, *Measurement*. 179 (2021) 109490. <https://doi.org/10.1016/J.MEASUREMENT.2021.109490>.
- [15] J.L. Chermant, M. Coster, Quantitative fractography, *Journal of Materials Science*. (1979). <https://doi.org/10.1007/BF00772710>.
- [16] G. Lesiuk, M. Szata, D. Rozumek, Z. Marciniak, J. Correia, A. de Jesus, Energy response of S355 and 41Cr4 steel during fatigue crack growth process, *Journal of Strain Analysis for Engineering Design*. (2018). <https://doi.org/10.1177/0309324718798234>.
- [17] R. Kosturek, L. Śniezek, J. Torzewski, M. Wachowski, Low Cycle Fatigue Properties of Sc-Modified AA2519-T62 Extrusion, *Materials* 2020, Vol. 13, Page 220. 13 (2020) 220. <https://doi.org/10.3390/MA13010220>.
- [18] T. Materials, *ASM Handbook, Volume 12, Fractography, Technology* (Singap World Sci). (2001). [https://doi.org/10.1016/S0026-0576\(03\)90166-8](https://doi.org/10.1016/S0026-0576(03)90166-8).
- [19] Q.Y. Deng, S.P. Zhu, J.C. He, X.K. Li, A. Carpinteri. Multiaxial fatigue under variable amplitude loadings: Review and solutions. *International Journal of Structural Integrity*, 2022, 13(3): 349-393.
- [20] M. Ghasemvand, B. Behjat, S. Ebrahimi, Experimental investigation of the effects of adhesive defects on the strength and creep behavior of single-lap adhesive joints at various temperatures, <https://doi.org/10.1080/00218464.2022.2095262>. (2022). <https://doi.org/10.1080/00218464.2022.2095262>.

- [21] W. Macek, A. Tomczyk, R. Branco, M. Dobrzyński, A. Seweryn, Fractographical quantitative analysis of EN-AW 2024 aluminum alloy after creep pre-strain and LCF loading, *Eng Fract Mech.* (2023) 109182. <https://doi.org/10.1016/J.ENGFRACMECH.2023.109182>.
- [22] G.L. Golewski, Measurement of fracture mechanics parameters of concrete containing fly ash thanks to use of Digital Image Correlation (DIC) method, *Measurement.* 135 (2019) 96–105. <https://doi.org/10.1016/J.MEASUREMENT.2018.11.032>.
- [23] H. Luo, L. Yu, B. Pan, Design and validation of a demand-oriented single-camera stereo-DIC system with a four-mirror adapter, *Measurement.* 186 (2021) 110083. <https://doi.org/10.1016/J.MEASUREMENT.2021.110083>.
- [24] E. Merson, V. Danilov, D. Merson, A. Vinogradov, Confocal laser scanning microscopy: The technique for quantitative fractographic analysis, *Engineering Fracture Mechanics.* (2017). <https://doi.org/10.1016/j.engfracmech.2017.04.026>.
- [25] Y. Wang, E.I. Meletis, H. Huang, Quantitative study of surface roughness evolution during low-cycle fatigue of 316L stainless steel using Scanning Whitelight Interferometric (SWLI) Microscopy, *International Journal of Fatigue.* (2013). <https://doi.org/10.1016/j.ijfatigue.2012.11.009>.
- [26] A. Gryguc, S.B. Behraves, S.K. Shaha, H. Jahed, M. Wells, B. Williams, X. Su, Low-cycle fatigue characterization and texture induced ratcheting behaviour of forged AZ80 Mg alloys, *International Journal of Fatigue.* 116 (2018) 429–438. <https://doi.org/10.1016/J.IJFATIGUE.2018.06.028>.
- [27] J. Jamali, A.-H.I. Mourad, Y. Fan, J.T. Wood, Through-thickness fracture behavior of unidirectional glass fibers/epoxy composites under various in-plane loading using the CTS test, *Engineering Fracture Mechanics.* 156 (2016) 83–95. <https://doi.org/10.1016/J.ENGFRACMECH.2016.01.016>.
- [28] A. Janeczek, J. Tomków, D. Fydrych, The Influence of Tool Shape and Process Parameters on the Mechanical Properties of AW-3004 Aluminium Alloy Friction Stir Welded Joints, *Materials* 2021, Vol. 14, Page 3244. 14 (2021) 3244. <https://doi.org/10.3390/MA14123244>.
- [29] D. Chuchala, M. Dobrzyński, D.Y. Pimenov, K.A. Orłowski, G. Krolczyk, K. Giasin, Surface Roughness Evaluation in Thin EN AW-6086-T6 Alloy Plates after Face Milling Process with Different Strategies, *Materials* 2021, Vol. 14, Page 3036. 14 (2021) 3036. <https://doi.org/10.3390/MA14113036>.
- [30] P. Podulka, A plateau-valley separation approach (PVSA) for reduction of the end-effect in surface metrology, *Measurement: Sensors.* 18 (2021) 100352. <https://doi.org/10.1016/J.MEASEN.2021.100352>.
- [31] W. Macek, D. Sampath, Ł. Pejkowski, K. Żak, A brief note on monotonic and fatigue fracture events investigation of thin-walled tubular austenitic steel specimens via fracture surface topography analysis (FRASTA), *Engineering Failure Analysis.* 134 (2022) 106048. <https://doi.org/10.1016/J.ENGFILANAL.2022.106048>.
- [32] Y.G. Cao, S.H. Zhang, K. Tanaka, Calculation method for maximum low-cycle fatigue loads using FRASTA reconstruction data, *International Journal of Fracture.* (2013). <https://doi.org/10.1007/s10704-013-9862-z>.
- [33] T. Kobayashi, D.A. Shockey, Fracture surface topography analysis (FRASTA)—Development, accomplishments, and future applications, *Engineering Fracture Mechanics.* 77 (2010) 2370–2384. <https://doi.org/10.1016/J.ENGFRACMECH.2010.05.016>.

- [34] A. Katunin, M. Zuba, Identification of Delamination in Composite Beams using the Fractal Dimension-Based Damage Identification Algorithm, *Fatigue of Aircraft Structures*. 2017 (2017) 5–16. <https://doi.org/10.1515/FAS-2017-0001>.
- [35] F. v. Antunes, D. Camas, L. Correia, R. Branco, Finite element meshes for optimal modelling of plasticity induced crack closure, *Engineering Fracture Mechanics*. 142 (2015) 184–200. <https://doi.org/10.1016/J.ENGFRACMECH.2015.06.007>.
- [36] S. Chen, W. Lu, J. Guo, D. Zhai, W. Chen, Flexible and high-resolution surface metrology based on stitching interference microscopy, *Optics and Lasers in Engineering*. 151 (2022) 106915. <https://doi.org/10.1016/J.OPTLASENG.2021.106915>.
- [37] J. Monnier, J. Zhu, Inference of the bottom topography in anisothermal mildly-sheared shallow ice flows, *Computer Methods in Applied Mechanics and Engineering*. 348 (2019) 954–977. <https://doi.org/10.1016/J.CMA.2019.01.003>.
- [38] G. Maculotti, E. Goti, G. Genta, L. Mazza, M. Galetto, Uncertainty-based comparison of conventional and surface topography-based methods for wear volume evaluation in pin-on-disc tribological test, *Tribology International*. 165 (2022) 107260. <https://doi.org/10.1016/J.TRIBOINT.2021.107260>.
- [39] C. Yu, Y. Bao, Q. Li, Finite element analysis of excavator mechanical behavior and boom structure optimization, *Measurement*. 173 (2021) 108637. <https://doi.org/10.1016/J.MEASUREMENT.2020.108637>.
- [40] S. Rakshe, S. V. Nimje, S.K. Panigrahi, Optimization of Adhesively Bonded Spar-Wingskin Joints of Laminated FRP Composites Subjected to Pull-Off Load: A Critical Review, *Progress in Adhesion and Adhesives*, Volume 6. (2021) 29–46. <https://doi.org/10.1002/9781119846703.CH2>.
- [41] W. Macek, R. Branco, J. Trembacz, J.D. Costa, J.A.M. Ferreira, C. Capela, Effect of multiaxial bending-torsion loading on fracture surface parameters in high-strength steels processed by conventional and additive manufacturing, *Engineering Failure Analysis*. 118 (2020). <https://doi.org/10.1016/j.engfailanal.2020.104784>.
- [42] R. Branco, J.D. Costa, J.A. Martins Ferreira, C. Capela, F. v. Antunes, W. Macek, Multiaxial fatigue behaviour of maraging steel produced by selective laser melting, *Materials and Design*. 201 (2021) 109469. <https://doi.org/10.1016/j.matdes.2021.109469>.
- [43] W. Macek, G. Robak, K. Żak, R. Branco, Fracture surface topography investigation and fatigue life assessment of notched austenitic steel specimens, *Engineering Failure Analysis*. 135 (2022) 106121. <https://doi.org/10.1016/J.ENGFAILANAL.2022.106121>.
- [44] W. Macek, Fractal analysis of the bending-torsion fatigue fracture of aluminium alloy, *Engineering Failure Analysis*. 99 (2019) 97–107. <https://doi.org/10.1016/j.engfailanal.2019.02.007>.
- [45] W. Macek, R. Branco, M. Korpyś, T. Łagoda, Fractal dimension for bending–torsion fatigue fracture characterisation, *Measurement*. 184 (2021) 109910. <https://doi.org/10.1016/J.MEASUREMENT.2021.109910>.
- [46] W. Macek, Correlation between Fractal Dimension and Areal Surface Parameters for Fracture Analysis after Bending-Torsion Fatigue, *Metals* 2021, Vol. 11, Page 1790. 11 (2021) 1790. <https://doi.org/10.3390/MET11111790>.



- [47] W. Macek, The impact of surface slope and calculation resolution on the fractal dimension for fractures of steels after bending-torsion fatigue, *Surface Topography: Metrology and Properties*. 10 (2022) 015030. <https://doi.org/10.1088/2051-672X/AC58AE>.
- [48] K. Mouralova, J. Kovar, L. Klakurkova, P. Blazik, M. Kalivoda, P. Kousal, Analysis of surface and subsurface layers after WEDM for Ti-6Al-4V with heat treatment, *Measurement*. 116 (2018) 556–564. <https://doi.org/10.1016/J.MEASUREMENT.2017.11.053>.
- [49] L. Pagani, X. Jiang, P.J. Scott, Investigation on the effect of sampling on areal texture parameters, *Measurement*. 128 (2018) 306–313. <https://doi.org/10.1016/J.MEASUREMENT.2018.06.052>.
- [50] J. Allum, A. Gleadall, V. V. Silberschmidt, Fracture of 3D-printed polymers: Crucial role of filament-scale geometric features, *Engineering Fracture Mechanics*. 224 (2020) 106818. <https://doi.org/10.1016/J.ENGFRACMECH.2019.106818>.
- [51] M. Kahlin, H. Ansell, D. Basu, A. Kerwin, L. Newton, B. Smith, J.J. Moverare, Improved fatigue strength of additively manufactured Ti6Al4V by surface post processing, *International Journal of Fatigue*. 134 (2020) 105497. <https://doi.org/10.1016/J.IJFATIGUE.2020.105497>.
- [52] W. Macek, R. Branco, J.D. Costa, J. Trembacz, Fracture Surface Behavior of 34CrNiMo6 High-Strength Steel Bars with Blind Holes under Bending-Torsion Fatigue, *Materials 2022*, Vol. 15, Page 80. 15 (2021) 80. <https://doi.org/10.3390/MA15010080>.
- [53] ISO - ISO 1101:2017 - Geometrical product specifications (GPS) — Geometrical tolerancing — Tolerances of form, orientation, location and run-out, (n.d.). <https://www.iso.org/standard/66777.html> (accessed December 12, 2021).
- [54] K. Brzeziński, K. Józefiak, A. Zbiciak, On the interpretation of shear parameters uncertainty with a linear regression approach, *Measurement*. 174 (2021) 108949. <https://doi.org/10.1016/J.MEASUREMENT.2020.108949>.
- [55] J.L. Kirschvink, The least-squares line and plane and the analysis of palaeomagnetic data, *Geophysical Journal International*. 62 (1980) 699–718. <https://doi.org/10.1111/J.1365-246X.1980.TB02601.X>.
- [56] W. Macek, R. Branco, J.D. Costa, J. Trembacz, Fracture Surface Behavior of 34CrNiMo6 High-Strength Steel Bars with Blind Holes under Bending-Torsion Fatigue, *Materials 2022*, Vol. 15, Page 80. 15 (2021) 80. <https://doi.org/10.3390/MA15010080>.
- [57] ISO - ISO 25178-2:2012 - Geometrical product specifications (GPS) — Surface texture: Areal — Part 2: Terms, definitions and surface texture parameters, (n.d.). <https://www.iso.org/standard/42785.html> (accessed December 28, 2020).

## CRediT authorship contribution statement

**W. Macek:** Conceptualization, Methodology, Formal analysis, Data curation, Investigation, Writing - Original Draft, Visualization.

**R. Branco:** Investigation, Formal analysis, Visualization, Writing - review & editing.

**P. Podulka:** Writing - review & editing.

**R. Masoudi Nejad:** Writing - review & editing.

**J.D. Costa:** Investigation.

**J.A.M. Ferreira:** Investigation.

**C. Capela:** Investigation.

**Declaration of interests**

The authors declare that they have no known competing financial interests or personal relationships that could have appeared to influence the work reported in this paper.

The authors declare the following financial interests/personal relationships which may be considered as potential competing interests:

**The correlation of fractal dimension to fracture surface slope for fatigue crack initiation analysis under bending-torsion loading in high-strength steels**

W. Macek<sup>a</sup>, R. Branco<sup>b</sup>, P. Podulka<sup>c</sup>, R. Masoudi Nejad<sup>d</sup>, J.D. Costa<sup>b</sup>, J.A.M. Ferreira<sup>b</sup>, C. Capela<sup>b,e</sup>

<sup>a</sup> Gdańsk University of Technology, Faculty of Mechanical Engineering and Ship Technology, Gdańsk, Poland

<sup>b</sup> University of Coimbra, CEMMPRE, Department of Mechanical Engineering, Coimbra, Portugal

<sup>c</sup> Rzeszow University of Technology, Faculty of Mechanical Engineering and Aeronautics, Rzeszów, Poland

<sup>d</sup> School of Mechanical and Electrical Engineering, University of Electronic Science and Technology of

